

Time-domain hybrid formulations for wave simulations in three-dimensional PML-truncated heterogeneous media

Arash Fathi¹, Babak Poursartip¹ and Loukas F. Kallivokas^{1,2,*,†}

¹*Department of Civil, Architectural and Environmental Engineering, The University of Texas at Austin, Austin, TX, USA*

²*The Institute for Computational Engineering and Sciences, The University of Texas at Austin, Austin, TX, USA*

SUMMARY

We are concerned with the numerical simulation of wave motion in arbitrarily heterogeneous, elastic, perfectly-matched-layer-(PML)-truncated media. We extend in three dimensions a recently developed two-dimensional formulation, by treating the PML via an unsplit-field, but mixed-field, displacement-stress formulation, which is then coupled to a standard displacement-only formulation for the interior domain, thus leading to a computationally cost-efficient hybrid scheme. The hybrid treatment leads to, at most, third-order in time semi-discrete forms. The formulation is flexible enough to accommodate the standard PML, as well as the multi-axial PML.

We discuss several time-marching schemes, which can be used à la carte, depending on the application: (a) an extended Newmark scheme for third-order in time, either unsymmetric or fully symmetric semi-discrete forms; (b) a standard implicit Newmark for the second-order, unsymmetric semi-discrete forms; and (c) an explicit Runge–Kutta scheme for a first-order in time unsymmetric system. The latter is well-suited for large-scale problems on parallel architectures, while the second-order treatment is particularly attractive for ready incorporation in existing codes written originally for finite domains.

We compare the schemes and report numerical results demonstrating stability and efficacy of the proposed formulations. Copyright © 2014 John Wiley & Sons, Ltd.

Received 11 April 2014; Revised 3 August 2014; Accepted 4 August 2014

KEY WORDS: unsplit-field perfectly-matched-layer (PML); elastic wave propagation; explicit time stepping; mixed finite elements; spectral element; hybrid formulation

1. INTRODUCTION

Numerical simulation of elastic waves in unbounded heterogeneous media has important applications in various fields, such as seismology [1], soil-structure interaction [2], seismic imaging [3], and site characterization [4]. To keep the computation feasible, one needs to limit the extent of the computational domain. This entails considering appropriate conditions at the truncation boundaries such that, under ideal conditions, the boundaries become invisible to the outgoing waves. Perfectly-matched-layers (PMLs) appear to be among the best choices for domain truncation owing, especially, to their ability to handle heterogeneity. From a practical standpoint, implementing PML in existing codes is also easier than competitive alternatives [5, 6]. The PML is a buffer zone that enforces attenuation of propagating and evanescent waves. The PML's properties vary gradually, from a perfectly matched interface through a progressively attenuative medium to, usually, a fixed termination at the buffer zone's end.[‡]

*Correspondence to: Loukas F. Kallivokas, The Institute for Computational Engineering and Sciences, The University of Texas at Austin, Austin, TX, USA.

†E-mail: loukas@mail.utexas.edu

‡Other termination conditions are also possible, including local non-reflecting boundary conditions [7, 8].

The PML was first introduced by Bérenger for electromagnetic waves [9]. Later, it was interpreted as a mapping of the physical coordinates onto the complex space, referred to as complex coordinate stretching [10–12]. The interpretation allowed the further development and adoption of the PML in elastodynamics [13, 14], for the linearized Euler equations [15], for Helmholtz equations [5], in poroelasticity [16], and elsewhere.

Bérenger's original development, and many other early formulations, was based on field-splitting, which partitions a physical variable into components parallel and perpendicular to the truncation boundary; this technique alters the structure of the underlying differential equations and results in a manyfold increase of the number of unknowns. Gedney proposed an unsplit formulation for electromagnetic waves, citing preservation of the Maxwellian structure, and computational efficiency among the main advantages [17]. Abarbanel and Gottlieb showed that Bérenger's split-form is only weakly well-posed[§] and therefore is prone to instability [19]. This motivated the development of strongly well-posed unsplit formulations [20]; however, it turned out that the dynamical system associated with the unsplit form suffers from degeneracy at quiescent state, which renders the scheme unstable, and further manipulation of the equations is necessary to ensure stability [21].

In elastodynamics, Duru and Kreiss [22] proposed a well-posed discretely stable unsplit formulation and mentioned that the first-order split-form is only weakly hyperbolic [23].[¶] Among other unsplit formulations, we refer to [24–26] where the authors' motivation stemmed primarily from exploring alternative forms, rather than address stability. All these developments used finite differences for spatial discretization and exploited explicit time-stepping. Among unsplit-field finite element developments, Basu and Chopra [2] presented an almost displacement-only procedure that relies on stress histories and needs the evaluation of an internal force vector at every time step, as is typically carried out in plasticity, via an implicit time-marching scheme based on unsymmetric matrices. Later, Basu [27] extended this work to three-dimensional problems, using mass-lumping and explicit time-stepping. Martin *et al.* [28] developed a computationally efficient procedure that couples a velocity-stress convolutional PML (CPML) in an ad hoc manner with a displacement-only formulation in the interior domain for two-dimensional problems. The CPML formulation was used to circumvent instabilities observed when waves travel along the interface between the PML and the interior domain, when the standard PML stretching function is used. Recently, Kucukcoban and Kallivokas [29] developed a symmetric displacement-stress formulation using mixed finite elements for the PML, coupled with standard displacement-only finite elements for the interior domain, using the standard Newmark method for time integration. We remark that implicit time-stepping can become challenging for large-scale three-dimensional problems and should be avoided if possible.

The literature on split-field elastodynamics is rich. This approach is particularly attractive because, normally, it does not use convolutions or auxiliary variables. However, it almost always results in using mixed schemes, that is, treating velocity and stress components (or a similar combination) as unknowns over the entire domain. Table I summarizes key developments in time-domain elastodynamics based on four categories: split-field or unsplit-field formulation and finite difference or finite/spectral element implementation.

Differences between various PML formulations are not only due to the split or unsplit formulation and numerical implementation but also on the choice of coordinate stretching function. The classical stretching function has been criticized for allowing spurious growths in numerical simulations in two dimensions, when waves impinge at grazing incidence on the PML interface. These growths have been loosely attributed to a zero-frequency singularity in the classical stretching function and have been reportedly alleviated by using a complex frequency-shifted (CFS) stretching function, which removes the singularity [24]. However the CFS-PML loses its absorptive competence at low frequencies [38]. Meza-Fajardo and Papageorgiou [37] proposed a multi-axial stretching approach and demonstrated its successful performance for waves traveling through the PML at grazing incidence as well as for problems involving anisotropy. In [39, 40], it was reported that the multi-axial perfectly matched layer (M-PML) is not perfectly matched at the interface; however, later on, Meza-Fajardo and Papageorgiou showed that the M-PML is indeed perfectly matched in Bérenger's sense

[§]See [18] for definition of well-posedness and hyperbolicity.

[¶]Strong hyperbolicity is a desirable property and guarantees well-posedness.

Table I. PML developments in time-domain elastodynamics.

	Split-field	Unsplit-field
FD	Chew and Liu [13] Hastings <i>et al.</i> [30] Liu [31] Collino and Tsogka [14]	Wang and Tang [26] Drossaert and Giannopoulos [24] Komatitsch and Martin [25] Duru and Kreiss [22]
FE/SE	Collino and Tsogka [14] Bécache <i>et al.</i> [32] Festa and Nielsen [33] Komatitsch and Tromp [34] Cohen and Fauqueux [35] Festa and Vilotte [36] Meza-Fajardo and Papageorgiou [37]	Basu and Chopra [2] Martin <i>et al.</i> [28] Basu [27] Kucukcoban and Kallivokas [29]

FD, finite difference; FE/SE, finite element/spectral element.

and it provides domain truncations that are at least as accurate as the classical PML, when the latter is stable [41]. In a more recent study, Ping *et al.* [42] have shown results according to which M-PML may perform less accurately than the classical PML. Our own experience, both in 2D and 3D simulations, is also more in accordance with Ping *et al.* [42]. It also seems that the original M-PML development is mathematically inconsistent because of the improper definition of the Jacobian of the transformation. We discuss this issue in Section 7. Herein, we opt for classical stretching functions for their simplicity, satisfactory performance when parametrized carefully, and their accuracy in low frequencies, which is important in site characterization problems [4]. We also discuss how our formulation can accommodate the multi-axial stretching through simple modifications.

In this article, we report on the development and parallel implementation of an unsplit-field displacement-stress PML formulation, using mixed finite elements for the PML, and coupled with standard displacement-only finite elements in the interior domain for three-dimensional problems in arbitrary heterogeneous elastic media. This hybrid treatment leads to optimal computational cost and allows for ready incorporation of the PML in existing standard finite element codes, by simply assembling matrices corresponding to the PML buffer. Using spectral elements, we render the mass matrix diagonal and exploit explicit time-stepping via the Runge–Kutta method. We also present an alternative formulation, which results in a fully symmetric discrete form, at the expense of utilizing an implicit time-marching scheme. We discuss how the standard Newmark scheme can also be used for time integration. This work builds and improves upon recent developments [29, 43] in two-dimensional elastodynamics.

2. COMPLEX COORDINATE STRETCHING

In this section, we briefly review the key features of the PML. Part of the material discussed here is not new; however, it is provided to allow for context and completeness.

2.1. Key idea

The key idea in constructing a PML is based on analytic continuation of solutions of wave equations. This amounts to mapping the spatial coordinates onto the complex space, using the, so-called, stretching functions. For instance, 1D outgoing waves propagate according to $u^{out}(x, t) = e^{-ik(x-ct)}$, where k is the wave number and c denotes wave speed. After applying the mapping^{||} $x \mapsto a(x) + \frac{1}{i\omega} b(x)$, we obtain $u_{PML}^{out}(x, t) = e^{-ik(a(x)-ct)} e^{-b(x)/c}$, where the latter term enforces spatial attenuation. A similar argument also holds for evanescent waves.

In practice, the PML has a limited thickness (Figure 1). Therefore, reflections (i.e., incoming waves) develop when outgoing waves hit the rigid boundary of the PML layer. In our 1D example,

^{||} $a(x), b(x)$ are positive, monotonically increasing functions of x .

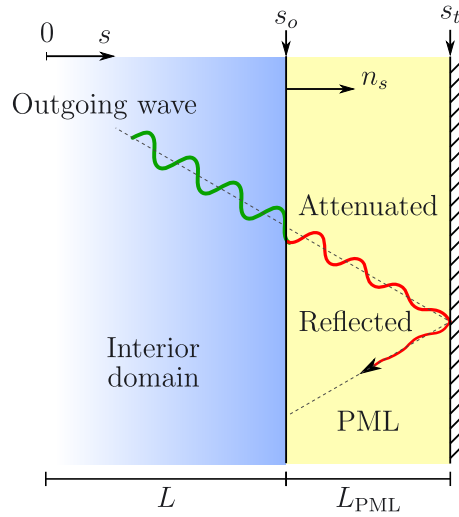


Figure 1. A PML truncation boundary in the direction of coordinate s .

$u_{\text{PML}}^{\text{inc}}(x, t) = e^{ik(a(x)+ct)} e^{b(x)/c}$. And, because $b(x)$ is positive, monotonically increasing function of x , where x decreases for incoming waves, reflected waves also get attenuated. Hence, the PML attenuates both outgoing and incoming waves.

We briefly discuss the principal components required for constructing a PML. Considering Figure 1, let s denote the coordinate variable normal to the interface of the interior domain with the PML. For the interior domain, it holds $0 < s < s_0$, whereas for the PML $s_0 < s < s_t$; L_{PML} denotes the thickness of the PML layer, and n_s is the outward unit normal at the interface, pointing away from the interior domain. The physical coordinate s is mapped (or ‘stretched’) to \tilde{s} within the PML region according to

$$s \mapsto \tilde{s} = s_0 + \int_{s_0}^s \lambda_s(s', \omega) ds', \tag{1}$$

where ω denotes circular frequency and λ_s is the, so-called, stretching function.

The classical PML results from choosing the stretching function according to

$$\lambda_s(s, \omega) = \alpha_s(s) + \frac{1}{i\omega} \beta_s(s), \tag{2}$$

where α_s is the scaling function and stretches the coordinate variable s , whereas β_s is the attenuation function and enforces the amplitude decay of propagating waves.** For evanescent waves, α_s improves amplitude decay by elongating the real coordinate variable s . For the interface to be ‘invisible’ to the waves entering the PML (perfect matching), $\alpha_s|_{s=s_0} = 1$ and $\beta_s|_{s=s_0} = 0$. Moreover, α_s and β_s are positive, non-decreasing functions of s . Finally, applying the fundamental theorem of calculus to (1), there results

$$\frac{d\tilde{s}}{ds} = \frac{d}{ds} \int_{s_0}^s \lambda_s(s', \omega) ds' = \lambda_s(s, \omega). \tag{3}$$

Hence, we obtain the following derivative rule between the stretched coordinate system and the physical coordinate system

$$\frac{d(\cdot)}{d\tilde{s}} = \frac{1}{\lambda_s(s, \omega)} \frac{d(\cdot)}{ds}. \tag{4}$$

**In our 1D example, we used the notation $a(x) = \int_0^x \alpha(x') dx'$ and $b(x) = \int_0^x \beta(x') dx'$.

The PML governing equations are naturally written in the stretched coordinate system. We frequently use (4) to express the PML equations in the physical coordinate system.

2.2. Choice of stretching functions

The main requirements for the stretching functions are as follows: (a) perfect matching at the interface; (b) positive non-decreasing variability; and (c) a gradual and smoothly varying profile. The last requirement is particularly important for numerical discretization, because, for adequate resolution, a sharply varying profile requires a finer mesh than a smoother profile. A widely adopted form that satisfies these requirements is given in terms of polynomials, as in

$$\alpha_s(s) = 1 + \alpha_o \left[\frac{(s - s_o)n_s}{L_{\text{PML}}} \right]^m, \quad s_o \leq s \leq s_t, \tag{5a}$$

$$\beta_s(s) = \beta_o \left[\frac{(s - s_o)n_s}{L_{\text{PML}}} \right]^m, \quad s_o \leq s \leq s_t, \tag{5b}$$

where α_o and β_o are user-tunable parameters that control amplitude decay and m denotes polynomial degree.

For one-dimensional problems, before discretization, β_o can be shown to be

$$\beta_o = \frac{(m + 1) c_p}{2 L_{\text{PML}}} \log \left(\frac{1}{R} \right), \tag{6}$$

where R is the amount of reflection from the outer PML boundary and c_p is the P-wave velocity. In practice, however, selecting appropriate values for α_o and β_o is not straightforward. The choice depends on the problem at hand, mesh resolution, and it, typically, needs a few experiments to be optimized. We remark that the performance of the PML relies heavily on its careful parameterization [7, 29].

We also worked with the following trigonometric profiles that are smoother than polynomials; however, we did not observe any compelling improvement.

$$\alpha_s(s) = 1 + \frac{\alpha_o}{2} \left[1 + \sin \left(\pi \left(\frac{|s - s_o|}{L_{\text{PML}}} - \frac{1}{2} \right) \right) \right], \quad s_o \leq s \leq s_t, \tag{7a}$$

$$\beta_s(s) = \frac{\beta_o}{2} \left[1 + \sin \left(\pi \left(\frac{|s - s_o|}{L_{\text{PML}}} - \frac{1}{2} \right) \right) \right], \quad s_o \leq s \leq s_t. \tag{7b}$$

3. THREE-DIMENSIONAL UNSPLIT-FIELD PML

The linear elastic wave equation, in the absence of body forces, can be written as the following system:

$$\mathbf{div} \mathcal{S}^T = \rho \ddot{\mathbf{u}}, \tag{8a}$$

$$\mathcal{S} = \mu [\nabla \mathbf{u} + (\nabla \mathbf{u})^T] + \lambda (\mathbf{div} \mathbf{u}) \mathcal{I}, \tag{8b}$$

where (8a) represents conservation of linear momentum and (8b) is the combined constitutive and kinematic equations; \mathcal{S} represents the Cauchy stress tensor, \mathbf{u} is the displacement vector, ρ denotes mass density of the medium, λ and μ are the two Lamé parameters, \mathcal{I} is the second-order identity tensor, and a dot (·) denotes differentiation with respect to time of the subtended variable.

To derive the corresponding PML equations, we first Fourier-transform (8) with respect to the time variable. Writing the resulting differential equations in the stretched coordinate system affords

the sought-after spatial decaying property. These equations can then be expressed in the physical coordinate system by using (4). Finally, exploiting the inverse Fourier transform results in the corresponding time-domain equations.

3.1. Frequency-domain equations

In this section, we present a PML formulation in the frequency domain. We take the Fourier transform of (8) with respect to the time variable; there results

$$\mathbf{div} \hat{\mathcal{S}}^T = (i\omega)^2 \rho \hat{\mathbf{u}}, \quad (9a)$$

$$\hat{\mathcal{S}} = \mu \left[\nabla \hat{\mathbf{u}} + (\nabla \hat{\mathbf{u}})^T \right] + \lambda (\mathbf{div} \hat{\mathbf{u}}) \mathcal{I}, \quad (9b)$$

where a caret (^) denotes the Fourier transform of the subtended variable, and spatial and frequency dependency of the variables are suppressed for brevity. We focus on (9a) first and express it in the stretched coordinate system by replacing x , y , and z with \tilde{x} , \tilde{y} , and \tilde{z} , respectively. For clarity, we use the unabridged notation:

$$\frac{\partial \hat{\mathcal{S}}_{xx}}{\partial \tilde{x}} + \frac{\partial \hat{\mathcal{S}}_{yx}}{\partial \tilde{y}} + \frac{\partial \hat{\mathcal{S}}_{zx}}{\partial \tilde{z}} = (i\omega)^2 \rho \hat{u}_x, \quad (10a)$$

$$\frac{\partial \hat{\mathcal{S}}_{xy}}{\partial \tilde{x}} + \frac{\partial \hat{\mathcal{S}}_{yy}}{\partial \tilde{y}} + \frac{\partial \hat{\mathcal{S}}_{zy}}{\partial \tilde{z}} = (i\omega)^2 \rho \hat{u}_y, \quad (10b)$$

$$\frac{\partial \hat{\mathcal{S}}_{xz}}{\partial \tilde{x}} + \frac{\partial \hat{\mathcal{S}}_{yz}}{\partial \tilde{y}} + \frac{\partial \hat{\mathcal{S}}_{zz}}{\partial \tilde{z}} = (i\omega)^2 \rho \hat{u}_z, \quad (10c)$$

where \mathcal{S}_{ij} and u_i denote stress tensor and displacement vector, respectively. Equation (10) can be expressed in the physical (unstretched) coordinate system by using (4); thus, we obtain

$$\frac{1}{\lambda_x} \frac{\partial \hat{\mathcal{S}}_{xx}}{\partial x} + \frac{1}{\lambda_y} \frac{\partial \hat{\mathcal{S}}_{yx}}{\partial y} + \frac{1}{\lambda_z} \frac{\partial \hat{\mathcal{S}}_{zx}}{\partial z} = (i\omega)^2 \rho \hat{u}_x, \quad (11a)$$

$$\frac{1}{\lambda_x} \frac{\partial \hat{\mathcal{S}}_{xy}}{\partial x} + \frac{1}{\lambda_y} \frac{\partial \hat{\mathcal{S}}_{yy}}{\partial y} + \frac{1}{\lambda_z} \frac{\partial \hat{\mathcal{S}}_{zy}}{\partial z} = (i\omega)^2 \rho \hat{u}_y, \quad (11b)$$

$$\frac{1}{\lambda_x} \frac{\partial \hat{\mathcal{S}}_{xz}}{\partial x} + \frac{1}{\lambda_y} \frac{\partial \hat{\mathcal{S}}_{yz}}{\partial y} + \frac{1}{\lambda_z} \frac{\partial \hat{\mathcal{S}}_{zz}}{\partial z} = (i\omega)^2 \rho \hat{u}_z. \quad (11c)$$

Multiplying (11) by $\lambda_x \lambda_y \lambda_z$ results in

$$\mathbf{div} \left(\hat{\mathcal{S}}^T \Lambda \right) = (i\omega)^2 \rho \lambda_x \lambda_y \lambda_z \hat{\mathbf{u}}, \quad (12)$$

where the stretching tensor Λ is defined as

$$\begin{aligned} \Lambda &= \begin{bmatrix} \lambda_y \lambda_z & 0 & 0 \\ 0 & \lambda_x \lambda_z & 0 \\ 0 & 0 & \lambda_x \lambda_y \end{bmatrix} = \begin{bmatrix} \alpha_y \alpha_z & 0 & 0 \\ 0 & \alpha_x \alpha_z & 0 \\ 0 & 0 & \alpha_x \alpha_y \end{bmatrix} \\ &+ \frac{1}{(i\omega)} \begin{bmatrix} \alpha_y \beta_z + \alpha_z \beta_y & 0 & 0 \\ 0 & \alpha_x \beta_z + \alpha_z \beta_x & 0 \\ 0 & 0 & \alpha_x \beta_y + \alpha_y \beta_x \end{bmatrix} \\ &+ \frac{1}{(i\omega)^2} \begin{bmatrix} \beta_y \beta_z & 0 & 0 \\ 0 & \beta_x \beta_z & 0 \\ 0 & 0 & \beta_x \beta_y \end{bmatrix} = \Lambda_e + \frac{1}{i\omega} \Lambda_p + \frac{1}{(i\omega)^2} \Lambda_w. \end{aligned} \quad (13)$$

We remark that within the interior domain, Λ_e reduces to the identity tensor, whereas Λ_p and Λ_w vanish identically. Substituting (13) and (2) in (12), rearranging and grouping similar terms, results in

$$\mathbf{div} \left(\hat{S}^T \Lambda_e + \frac{1}{i\omega} \hat{S}^T \Lambda_p + \frac{1}{(i\omega)^2} \hat{S}^T \Lambda_w \right) = \rho \left[(i\omega)^2 a \hat{\mathbf{u}} + i\omega b \hat{\mathbf{u}} + c \hat{\mathbf{u}} + \frac{d}{i\omega} \hat{\mathbf{u}} \right], \quad (14)$$

where

$$\begin{aligned} a &= \alpha_x \alpha_y \alpha_z, \\ b &= \alpha_x \alpha_y \beta_z + \alpha_x \alpha_z \beta_y + \alpha_y \alpha_z \beta_x, \\ c &= \alpha_x \beta_y \beta_z + \alpha_y \beta_z \beta_x + \alpha_z \beta_y \beta_x, \\ d &= \beta_x \beta_y \beta_z. \end{aligned} \quad (15)$$

Multiplying (14) by $i\omega$, we obtain

$$\mathbf{div} \left(i\omega \hat{S}^T \Lambda_e + \hat{S}^T \Lambda_p + \frac{1}{i\omega} \hat{S}^T \Lambda_w \right) = \rho \left[(i\omega)^3 a \hat{\mathbf{u}} + (i\omega)^2 b \hat{\mathbf{u}} + i\omega c \hat{\mathbf{u}} + d \hat{\mathbf{u}} \right]. \quad (16)$$

Next, we focus our attention on the combined constitutive and kinematic Equations (9b). By writing (9b) in the stretched coordinate system and by using (4) to express it in the physical coordinate system, there results

$$\begin{aligned} \hat{S} &= \mu \left\{ (\nabla \hat{\mathbf{u}}) \begin{bmatrix} \frac{1}{\lambda_x} & 0 & 0 \\ 0 & \frac{1}{\lambda_y} & 0 \\ 0 & 0 & \frac{1}{\lambda_z} \end{bmatrix} + \begin{bmatrix} \frac{1}{\lambda_x} & 0 & 0 \\ 0 & \frac{1}{\lambda_y} & 0 \\ 0 & 0 & \frac{1}{\lambda_z} \end{bmatrix} (\nabla \hat{\mathbf{u}})^T \right\} \\ &\quad + \lambda \left(\frac{1}{\lambda_x} \frac{\partial \hat{u}_x}{\partial x} + \frac{1}{\lambda_y} \frac{\partial \hat{u}_y}{\partial y} + \frac{1}{\lambda_z} \frac{\partial \hat{u}_z}{\partial z} \right) \mathcal{I}. \end{aligned} \quad (17)$$

Multiplying (17) by $\lambda_x \lambda_y \lambda_z$ results in

$$\lambda_x \lambda_y \lambda_z \hat{S} = \mu \left[\nabla \hat{\mathbf{u}} \Lambda + \Lambda (\nabla \hat{\mathbf{u}})^T \right] + \lambda \operatorname{div} (\Lambda \hat{\mathbf{u}}) \mathcal{I}, \quad (18)$$

where the stretching tensor Λ is defined in (13). Multiplying (18) by $(i\omega)^2$ and using (13) and (2), rearranging and grouping similar terms, we obtain

$$\begin{aligned} (i\omega)^2 a \hat{S} + i\omega b \hat{S} + c \hat{S} + \frac{1}{i\omega} d \hat{S} &= \mu (i\omega)^2 \left[(\nabla \hat{\mathbf{u}}) \Lambda_e + \Lambda_e (\nabla \hat{\mathbf{u}})^T \right] \\ &\quad + \mu i\omega \left[(\nabla \hat{\mathbf{u}}) \Lambda_p + \Lambda_p (\nabla \hat{\mathbf{u}})^T \right] + \mu \left[(\nabla \hat{\mathbf{u}}) \Lambda_w + \Lambda_w (\nabla \hat{\mathbf{u}})^T \right] \\ &\quad + \lambda (i\omega)^2 \operatorname{div} (\Lambda_e \hat{\mathbf{u}}) \mathcal{I} + \lambda i\omega \operatorname{div} (\Lambda_p \hat{\mathbf{u}}) \mathcal{I} + \lambda \operatorname{div} (\Lambda_w \hat{\mathbf{u}}) \mathcal{I}. \end{aligned} \quad (19)$$

Equations (16) and (19) constitute the corresponding frequency-domain momentum, and combined constitutive and kinematic equations in the stretched coordinate system, respectively. They possess the desired spatial decaying property.

3.2. Time-domain equations

In this section, we apply the inverse Fourier transform to (16) and (19) to obtain the corresponding time-domain equations. This operation is rather simple because of the specific choice of the stretching function (2). We use

$$\mathcal{F}^{-1} \left[\frac{\hat{g}(\omega)}{i\omega} \right] = \int_0^t g(\tau) d\tau, \quad (20)$$

where \mathcal{F}^{-1} denotes the inverse Fourier-transform operator^{††} and $g(t)$ is a sufficiently regular function. By applying the inverse Fourier transform to (16) and (19), we obtain

$$\operatorname{div} \left[\dot{S}^T \Lambda_e + S^T \Lambda_p + \left(\int_0^t S^T d\tau \right) \Lambda_w \right] = \rho (a\ddot{\mathbf{u}} + b\dot{\mathbf{u}} + c\mathbf{u} + d\mathbf{u}), \quad (21a)$$

$$\begin{aligned} & a\ddot{S} + b\dot{S} + cS + d \left(\int_0^t S d\tau \right) \\ &= \mu \left[(\nabla\ddot{\mathbf{u}}) \Lambda_e + \Lambda_e (\nabla\dot{\mathbf{u}})^T + (\nabla\dot{\mathbf{u}}) \Lambda_p + \Lambda_p (\nabla\mathbf{u})^T + (\nabla\mathbf{u}) \Lambda_w + \Lambda_w (\nabla\mathbf{u})^T \right] \\ &+ \lambda \left[\operatorname{div} (\Lambda_e \ddot{\mathbf{u}}) + \operatorname{div} (\Lambda_p \dot{\mathbf{u}}) + \operatorname{div} (\Lambda_w \mathbf{u}) \right] \mathcal{I}. \end{aligned} \quad (21b)$$

The set of integro-differential equations (21) can be expressed as a set of only partial differential equations, upon introducing auxiliary variable $\mathbf{S}(\mathbf{x}, t)$, which may be interpreted as stress history [43, 44]:

$$\mathbf{S}(\mathbf{x}, t) = \int_0^t \mathcal{S}(\mathbf{x}, \tau) d\tau. \quad (22a)$$

Clearly,

$$\dot{\mathbf{S}}(\mathbf{x}, t) = \mathcal{S}(\mathbf{x}, t), \quad \ddot{\mathbf{S}}(\mathbf{x}, t) = \dot{\mathcal{S}}(\mathbf{x}, t), \quad \ddot{\mathbf{S}}(\mathbf{x}, t) = \ddot{\mathcal{S}}(\mathbf{x}, t). \quad (22b)$$

By substituting (22) in (21), we obtain

$$\operatorname{div} \left(\dot{S}^T \Lambda_e + \dot{\mathbf{S}}^T \Lambda_p + S^T \Lambda_w \right) = \rho (a\ddot{\mathbf{u}} + b\dot{\mathbf{u}} + c\mathbf{u} + d\mathbf{u}), \quad (23a)$$

$$\begin{aligned} & a\ddot{\mathbf{S}} + b\dot{\mathbf{S}} + c\mathbf{S} + d\mathbf{S} \\ &= \mu \left[(\nabla\ddot{\mathbf{u}}) \Lambda_e + \Lambda_e (\nabla\dot{\mathbf{u}})^T + (\nabla\dot{\mathbf{u}}) \Lambda_p + \Lambda_p (\nabla\mathbf{u})^T + (\nabla\mathbf{u}) \Lambda_w + \Lambda_w (\nabla\mathbf{u})^T \right] \\ &+ \lambda \left[\operatorname{div} (\Lambda_e \ddot{\mathbf{u}}) + \operatorname{div} (\Lambda_p \dot{\mathbf{u}}) + \operatorname{div} (\Lambda_w \mathbf{u}) \right] \mathcal{I}. \end{aligned} \quad (23b)$$

Equations (23) constitute the corresponding time-domain PML momentum, and combined constitutive and kinematic equations.

4. HYBRID FINITE ELEMENT IMPLEMENTATION

In this section, we discuss an efficient finite element technique for transient elastodynamics in PML-truncated domains. We use a method-of-lines approach, where we exploit a Galerkin method for spatial discretization, thus obtaining a third-order, continuous-in-time system of ordinary differential equations. Various methods exist for time integration of such systems. We discuss three techniques that seem suitable in practical applications.

4.1. Spatial discretization

The PML Equation (23) can be used both for the interior domain and the PML buffer zone, because by construction, they reduce to (8) in the interior domain. This unified treatment amounts to considering stress and displacement components as unknowns in both the interior domain and the PML buffer zone. While feasible in principle, as is carried out in most PML formulations to date, we opt for a hybrid treatment, originally developed in [29] for 2D problems, where the interior domain

^{††}In general, $\mathcal{F}^{-1} \left[\frac{\hat{g}(\omega)}{i\omega} \right] = \int_0^t g(\tau) d\tau - \pi \hat{g}(0) \delta(\omega)$, but it can be shown that because, by construction, the overall development excludes $\omega = 0$, the inverse transform reduces to (20) [43].

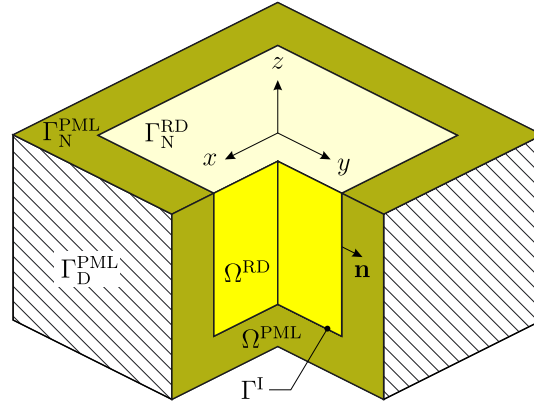


Figure 2. The PML-truncated semi-infinite domain.

is treated with a standard displacement-only formulation, coupled with the PML equations in the buffer zone. This approach results in substantial reduction in computational cost compared with mixed formulations cast over the entire domain. It also makes the modification of existing interior-domain elastodynamic codes straightforward, because one needs to only add the PML-related forms, whereas for the most part, the general structure of such codes remains intact.

Accordingly, find $\mathbf{u}(\mathbf{x}, t)$ in $\Omega^{RD} \cup \Omega^{PML}$ and $\mathbf{S}(\mathbf{x}, t)$ in Ω^{PML} (see Figure 2 for domain and boundary designations), where \mathbf{u} and \mathbf{S} reside in appropriate function spaces and

$$\mathbf{div} \left\{ \mu \left[\nabla \dot{\mathbf{u}} + (\nabla \dot{\mathbf{u}})^T \right] + \lambda (\text{div } \dot{\mathbf{u}}) \mathcal{I} \right\} + \dot{\mathbf{b}} = \rho \ddot{\mathbf{u}} \quad \text{in } \Omega^{RD} \times \mathbf{J}, \quad (24a)$$

$$\mathbf{div} \left(\ddot{\mathbf{S}}^T \Lambda_e + \dot{\mathbf{S}}^T \Lambda_p + \mathbf{S}^T \Lambda_w \right) = \rho (a \ddot{\mathbf{u}} + b \dot{\mathbf{u}} + c \mathbf{u} + d \mathbf{u}) \quad \text{in } \Omega^{PML} \times \mathbf{J}, \quad (24b)$$

$$\begin{aligned} & a \ddot{\mathbf{S}} + b \dot{\mathbf{S}} + c \mathbf{S} + d \mathbf{S} \\ &= \mu \left[(\nabla \ddot{\mathbf{u}}) \Lambda_e + \Lambda_e (\nabla \ddot{\mathbf{u}})^T + (\nabla \dot{\mathbf{u}}) \Lambda_p + \Lambda_p (\nabla \dot{\mathbf{u}})^T + (\nabla \mathbf{u}) \Lambda_w + \Lambda_w (\nabla \mathbf{u})^T \right] \\ & \quad + \lambda \left[\text{div} (\Lambda_e \ddot{\mathbf{u}}) + \text{div} (\Lambda_p \dot{\mathbf{u}}) + \text{div} (\Lambda_w \mathbf{u}) \right] \mathcal{I} \quad \text{in } \Omega^{PML} \times \mathbf{J}. \end{aligned} \quad (24c)$$

The system is initially at rest and subject to the following boundary and interface conditions:

$$\left\{ \mu \left[\nabla \dot{\mathbf{u}} + (\nabla \dot{\mathbf{u}})^T \right] + \lambda (\text{div } \dot{\mathbf{u}}) \mathcal{I} \right\} \mathbf{n}^+ = \dot{\mathbf{g}}_n \quad \text{on } \Gamma_N^{RD} \times \mathbf{J}, \quad (25a)$$

$$\left(\ddot{\mathbf{S}}^T \Lambda_e + \dot{\mathbf{S}}^T \Lambda_p + \mathbf{S}^T \Lambda_w \right) \mathbf{n}^- = \mathbf{0} \quad \text{on } \Gamma_N^{PML} \times \mathbf{J}, \quad (25b)$$

$$\mathbf{u} = \mathbf{0} \quad \text{on } \Gamma_D^{PML} \times \mathbf{J}, \quad (25c)$$

$$\mathbf{u}^+ = \mathbf{u}^- \quad \text{on } \Gamma^I \times \mathbf{J}, \quad (25d)$$

$$\left\{ \mu \left[\nabla \dot{\mathbf{u}} + (\nabla \dot{\mathbf{u}})^T \right] + \lambda (\text{div } \dot{\mathbf{u}}) \mathcal{I} \right\} \mathbf{n}^+ + \left(\ddot{\mathbf{S}}^T \Lambda_e + \dot{\mathbf{S}}^T \Lambda_p + \mathbf{S}^T \Lambda_w \right) \mathbf{n}^- = \mathbf{0} \quad \text{on } \Gamma^I \times \mathbf{J}, \quad (25e)$$

where temporal and spatial dependencies are suppressed for brevity; Ω^{RD} denotes the interior (regular) domain, Ω^{PML} represents the region occupied by the PML buffer zone, Γ^I is the interface boundary between the interior and PML domains, Γ_N^{RD} and Γ_N^{PML} denote the free (top surface) boundary of the interior domain and PML, respectively, and $\mathbf{J} = (0, T]$ is the time interval of interest. In (24a), \mathbf{b} denotes body force per unit volume.

We remark that the temporal differentiation in (24a) is necessary for the boundary integrals that result from the weak form of (24a) and (24b) to cancel out; this is manifested in (25e) and enforces

the balance of tractions at the interface of the interior domain and the PML. Moreover, (25d) implies continuity of displacements at the interface; (25a) specifies tractions (\mathbf{g}_n) on the top surface of the interior domain, and (25b) implies traction-free boundary condition on the top PML surface. We consider fixed boundaries for the PML on the sides and at the bottom, as indicated by (25c); other possibilities also exist, but they seem to have little influence on performance [7, 8].

Next, we seek a weak solution, corresponding to the strong form of (24) and (25), in the Galerkin sense. Specifically, we take the inner products of (24a) and (24b) with (vector) test function $\mathbf{w}(\mathbf{x})$ and integrate by parts over their corresponding domains. Incorporating (25d)–(25e) eliminates the interface boundary terms and results in (26a). Next, we take the inner product of (24c) with (tensor) test function $\mathbf{T}(\mathbf{x})$; there results (26b). There are other possibilities for deriving a weak form that corresponds to the strong form (24) and (25). We refer in [45] for further details.

Accordingly, find $\mathbf{u} \in \mathbf{H}^1(\Omega) \times \mathbf{J}$ and $\mathbf{S} \in \mathcal{L}^2(\Omega) \times \mathbf{J}$, such that

$$\int_{\Omega^{\text{RD}}} \nabla \mathbf{w} : \left\{ \mu \left[\nabla \dot{\mathbf{u}} + (\nabla \dot{\mathbf{u}})^T \right] + \lambda (\text{div } \dot{\mathbf{u}}) \mathcal{I} \right\} d\Omega + \int_{\Omega^{\text{PML}}} \nabla \mathbf{w} : \left(\ddot{\mathbf{S}}^T \Lambda_e + \dot{\mathbf{S}}^T \Lambda_p + \mathbf{S}^T \Lambda_w \right) d\Omega + \int_{\Omega^{\text{RD}}} \mathbf{w} \cdot \rho \ddot{\mathbf{u}} d\Omega + \int_{\text{PML}} \mathbf{w} \cdot \rho (a\ddot{\mathbf{u}} + b\dot{\mathbf{u}} + c\dot{\mathbf{u}} + d\mathbf{u}) d\Omega = \int_{\Gamma_N^{\text{RD}}} \mathbf{w} \cdot \dot{\mathbf{g}}_n d\Gamma + \int_{\Omega^{\text{RD}}} \mathbf{w} \cdot \dot{\mathbf{b}} d\Omega, \tag{26a}$$

$$\int_{\Omega^{\text{PML}}} \mathbf{T} : (a\ddot{\mathbf{S}} + b\dot{\mathbf{S}} + c\dot{\mathbf{S}} + d\mathbf{S}) d\Omega = \int_{\Omega^{\text{PML}}} \mathbf{T} : \mu \left[(\nabla \ddot{\mathbf{u}}) \Lambda_e + \Lambda_e (\nabla \ddot{\mathbf{u}})^T + (\nabla \dot{\mathbf{u}}) \Lambda_p + \Lambda_p (\nabla \dot{\mathbf{u}})^T + (\nabla \mathbf{u}) \Lambda_w + \Lambda_w (\nabla \mathbf{u})^T \right] + \mathbf{T} : \lambda \left[\text{div} (\Lambda_e \ddot{\mathbf{u}}) + \text{div} (\Lambda_p \dot{\mathbf{u}}) + \text{div} (\Lambda_w \mathbf{u}) \right] \mathcal{I} d\Omega, \tag{26b}$$

for every $\mathbf{w} \in \mathbf{H}^1(\Omega)$ and $\mathbf{T} \in \mathcal{L}^2(\Omega)$, where $\mathbf{g}_n \in \mathbf{L}^2(\Omega) \times \mathbf{J}$ and $\mathbf{b} \in \mathbf{L}^2(\Omega) \times \mathbf{J}$. Function spaces for scalar-valued (v), vector-valued (\mathbf{v}), and tensor-valued (\mathcal{A}) functions are defined as

$$L^2(\Omega) = \left\{ v : \int_{\Omega} |v|^2 d\mathbf{x} < \infty \right\}, \tag{27a}$$

$$\mathbf{L}^2(\Omega) = \{ \mathbf{v} : \mathbf{v} \in (L^2(\Omega))^3 \}, \tag{27b}$$

$$\mathcal{L}^2(\Omega) = \{ \mathcal{A} : \mathcal{A} \in (L^2(\Omega))^{3 \times 3} \}, \tag{27c}$$

$$H^1(\Omega) = \left\{ v : \int_{\Omega} (|v|^2 + |\nabla v|^2) d\mathbf{x} < \infty, v|_{\Gamma_D^{\text{PML}}} = 0 \right\}, \tag{27d}$$

$$\mathbf{H}^1(\Omega) = \{ \mathbf{v} : \mathbf{v} \in (H^1(\Omega))^3 \}. \tag{27e}$$

In order to resolve (26) numerically, we use standard finite-dimensional subspaces. Specifically, we introduce finite-dimensional subspaces $\Xi_h \subset \mathbf{H}^1(\Omega)$ and $\Upsilon_h \subset \mathcal{L}^2(\Omega)$, with basis functions Φ and Ψ , respectively. We then approximate $\mathbf{u}(\mathbf{x}, t)$ with $\mathbf{u}_h(\mathbf{x}, t) \in \Xi_h \times \mathbf{J}$ and $\mathbf{S}(\mathbf{x}, t)$ with $\mathbf{S}_h(\mathbf{x}, t) \in \Upsilon_h \times \mathbf{J}$, as detailed in (28)

$$\mathbf{u}_h(\mathbf{x}, t) = \begin{bmatrix} \Phi^T(\mathbf{x}) \mathbf{u}_x(t) \\ \Phi^T(\mathbf{x}) \mathbf{u}_y(t) \\ \Phi^T(\mathbf{x}) \mathbf{u}_z(t) \end{bmatrix}, \tag{28a}$$

$$\mathbf{S}_h(\mathbf{x}, t) = \begin{bmatrix} \Psi^T(\mathbf{x}) \mathbf{S}_{xx}(t) & \Psi^T(\mathbf{x}) \mathbf{S}_{xy}(t) & \Psi^T(\mathbf{x}) \mathbf{S}_{xz}(t) \\ \Psi^T(\mathbf{x}) \mathbf{S}_{yx}(t) & \Psi^T(\mathbf{x}) \mathbf{S}_{yy}(t) & \Psi^T(\mathbf{x}) \mathbf{S}_{yz}(t) \\ \Psi^T(\mathbf{x}) \mathbf{S}_{zx}(t) & \Psi^T(\mathbf{x}) \mathbf{S}_{zy}(t) & \Psi^T(\mathbf{x}) \mathbf{S}_{zz}(t) \end{bmatrix}. \tag{28b}$$

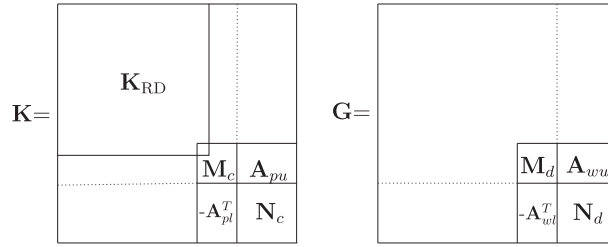


Figure 3. Partitioning of submatrices in (31b).

In a similar fashion, we approximate the test functions, $\mathbf{w}(\mathbf{x})$ with $\mathbf{w}_h(\mathbf{x}) \in \Xi_h$ and $\mathbf{T}(\mathbf{x})$ with $\mathbf{T}_h(\mathbf{x}) \in \Upsilon_h$; therefore,

$$\mathbf{w}_h(\mathbf{x}) = \begin{bmatrix} \mathbf{w}_x^T \Phi(\mathbf{x}) \\ \mathbf{w}_y^T \Phi(\mathbf{x}) \\ \mathbf{w}_z^T \Phi(\mathbf{x}) \end{bmatrix}, \quad (29a)$$

$$\mathbf{T}_h(\mathbf{x}) = \begin{bmatrix} \mathbf{T}_{xx}^T \Psi(\mathbf{x}) & \mathbf{T}_{xy}^T \Psi(\mathbf{x}) & \mathbf{T}_{xz}^T \Psi(\mathbf{x}) \\ \mathbf{T}_{yx}^T \Psi(\mathbf{x}) & \mathbf{T}_{yy}^T \Psi(\mathbf{x}) & \mathbf{T}_{yz}^T \Psi(\mathbf{x}) \\ \mathbf{T}_{zx}^T \Psi(\mathbf{x}) & \mathbf{T}_{zy}^T \Psi(\mathbf{x}) & \mathbf{T}_{zz}^T \Psi(\mathbf{x}) \end{bmatrix}. \quad (29b)$$

Incorporating (28)–(29) into (26) results in the following semi-discrete form:

$$\mathbf{M}\ddot{\mathbf{d}} + \mathbf{C}\dot{\mathbf{d}} + \mathbf{K}\mathbf{d} + \mathbf{G}\mathbf{d} = \mathbf{f}, \quad (30)$$

where spatial and temporal dependencies are suppressed for brevity and system matrices, \mathbf{M} , \mathbf{C} , \mathbf{K} , \mathbf{G} , and vectors \mathbf{d} and \mathbf{f} , are defined as

$$\mathbf{M} = \begin{bmatrix} \bar{\mathbf{M}}_{RD} + \bar{\mathbf{M}}_a & \mathbf{0} \\ \mathbf{0} & \mathbf{N}_a \end{bmatrix}, \quad \mathbf{C} = \begin{bmatrix} \bar{\mathbf{M}}_b & \bar{\mathbf{A}}_{eu} \\ -\bar{\mathbf{A}}_{el}^T & \mathbf{N}_b \end{bmatrix}, \quad (31a)$$

$$\mathbf{K} = \begin{bmatrix} \bar{\mathbf{K}}_{RD} + \bar{\mathbf{M}}_c & \bar{\mathbf{A}}_{pu} \\ -\bar{\mathbf{A}}_{pl}^T & \mathbf{N}_c \end{bmatrix}, \quad \mathbf{G} = \begin{bmatrix} \bar{\mathbf{M}}_d & \bar{\mathbf{A}}_{wu} \\ -\bar{\mathbf{A}}_{wl}^T & \mathbf{N}_d \end{bmatrix}, \quad (31b)$$

$$\mathbf{d} = [\mathbf{U} \ \boldsymbol{\Sigma}]^T, \quad \mathbf{f} = [\bar{\mathbf{f}}_{RD} \ \mathbf{0}]^T, \quad (31c)$$

where subscript RD refers to the interior (regular) domain and \mathbf{M}_{RD} , \mathbf{K}_{RD} , and \mathbf{f}_{RD} correspond to the standard mass matrix, stiffness matrix, and vector of nodal forces in the interior domain, respectively, and a bar indicates their extension to encompass all the displacement degrees-of-freedom^{‡‡}; \mathbf{U} and $\boldsymbol{\Sigma}$ is the vector of nodal displacements and stresses, respectively. Moreover, \mathbf{U} is partitioned such that its first entries belong solely to the interior domain, followed by those on the interface boundary between the interior domain and the PML buffer, and finally those that are located only within the PML. The rest of the submatrices in (31) correspond to the PML buffer zone (see Figure 3 for a schematic partitioning and Appendix A.1 for submatrix definition; the dotted line in Figure 3 separates displacement from stress degrees-of-freedom).

We remark that the upper-left corner blocks of \mathbf{M} and \mathbf{K} correspond to the mass and stiffness matrices of a standard displacement-only formulation, as depicted in Figure 3. This implies that in order to accommodate PML capability into existing codes, one needs to account for the submatrices on the lower-right blocks of \mathbf{M} , \mathbf{C} , \mathbf{K} , and \mathbf{G} .

The matrix \mathbf{M} has a block-diagonal structure ((A.2a)–(A.2c)); thus, it can be diagonalized if one employs spectral elements, which then enables explicit time integration of (30); this is discussed in Section 5.

^{‡‡}This is merely a formalism to arrive at a unified, yet informative, matrix representation. For instance, we take \mathbf{K}_{RD} and extend it by adding zero entries corresponding to the U components of the PML buffer. This makes the matrix–vector operation $\mathbf{K}_{RD} \mathbf{U}$ meaningful, where, now, \mathbf{U} contains the displacement degrees-of-freedom of the entire domain.

Notice that the semi-discrete form (30) is not symmetric. In fact, a block-diagonal structure for \mathbf{M} comes at the price of losing symmetry. Alternatively, one may preserve symmetry of the matrices in the semi-discrete form at the expense of losing the block-diagonal form of \mathbf{M} and thus the ability for explicit time integration. We discuss this alternative formulation in Section 6.

4.2. Discretization in time

In this section, we discuss various possibilities of integrating the semi-discrete form (30) in time. One may apply a time-marching scheme directly to (30), which is third-order in time, or exploit a more common scheme by first expressing (30) as a second-order or first-order in time system, via the introduction of auxiliary vectors.

Time integration can be accomplished by working with either (30) or one of its second-order or first-order system counterparts, or, alternatively, one may (analytically) integrate (30) in time first, to obviate the temporal differentiation of the forcing vector. Assuming the system is initially at rest, there results

$$\mathbf{M}\ddot{\mathbf{d}} + \mathbf{C}\dot{\mathbf{d}} + \mathbf{K}\mathbf{d} + \mathbf{G}\bar{\mathbf{d}} = \mathbf{f}, \quad (32a)$$

$$\bar{\mathbf{d}} = \int_0^t \mathbf{d}(\tau)|_{\text{PML}} d\tau, \quad (32b)$$

where $\bar{\mathbf{d}}$ is the vector of history terms. Equation (32) can be integrated via an extended Newmark method as outlined in Appendix B.2. The scheme is implicit and requires matrix factorization.

We remark that $\bar{\mathbf{d}}$ contains displacement and stress degrees-of-freedom that are associated with the PML buffer only; therefore, its size is much smaller than \mathbf{d} (Figure 3).

Alternatively, (32) can be expressed as a second-order system

$$\mathbf{M}\ddot{\mathbf{d}} + \mathbf{C}\dot{\mathbf{d}} + \mathbf{K}\mathbf{d} + \mathbf{G}\bar{\mathbf{d}} = \mathbf{f}, \quad (33a)$$

$$\dot{\bar{\mathbf{d}}} = \mathbf{d}|_{\text{PML}}. \quad (33b)$$

In matrix notation, (33) reads

$$\begin{bmatrix} \mathbf{M} & \mathbf{0} \\ \mathbf{0} & \mathbf{0} \end{bmatrix} \begin{bmatrix} \ddot{\mathbf{d}} \\ \ddot{\bar{\mathbf{d}}} \end{bmatrix} + \begin{bmatrix} \mathbf{C} & \mathbf{0} \\ \mathbf{0} & \mathbf{I} \end{bmatrix} \begin{bmatrix} \dot{\mathbf{d}} \\ \dot{\bar{\mathbf{d}}} \end{bmatrix} + \begin{bmatrix} \mathbf{K} & \mathbf{G} \\ -\mathbf{I} & \mathbf{0} \end{bmatrix} \begin{bmatrix} \mathbf{d} \\ \bar{\mathbf{d}} \end{bmatrix} = \begin{bmatrix} \mathbf{f} \\ \mathbf{0} \end{bmatrix}, \quad (34)$$

where now a standard Newmark scheme may be utilized to integrate (34); or alternatively

$$\begin{bmatrix} \mathbf{M} & \mathbf{0} \\ \mathbf{0} & \mathbf{I} \end{bmatrix} \begin{bmatrix} \ddot{\mathbf{d}} \\ \ddot{\bar{\mathbf{d}}} \end{bmatrix} + \begin{bmatrix} \mathbf{C} & \mathbf{0} \\ -\mathbf{I} & \mathbf{0} \end{bmatrix} \begin{bmatrix} \dot{\mathbf{d}} \\ \dot{\bar{\mathbf{d}}} \end{bmatrix} + \begin{bmatrix} \mathbf{K} & \mathbf{G} \\ \mathbf{0} & \mathbf{0} \end{bmatrix} \begin{bmatrix} \mathbf{d} \\ \bar{\mathbf{d}} \end{bmatrix} = \begin{bmatrix} \mathbf{f} \\ \mathbf{0} \end{bmatrix}, \quad (35)$$

where the resulting system can be integrated explicitly, provided that \mathbf{M} is diagonal, as we discuss in Section 5.

One may also express (32) as a first-order system

$$\frac{d}{dt} \begin{bmatrix} \mathbf{x}_0 \\ \mathbf{x}_1 \\ \mathbf{M}\mathbf{x}_2 \end{bmatrix} = \begin{bmatrix} \mathbf{0} & \mathbf{I} & \mathbf{0} \\ \mathbf{0} & \mathbf{0} & \mathbf{I} \\ -\mathbf{G} & -\mathbf{K} & -\mathbf{C} \end{bmatrix} \begin{bmatrix} \mathbf{x}_0 \\ \mathbf{x}_1 \\ \mathbf{x}_2 \end{bmatrix} + \begin{bmatrix} \mathbf{0} \\ \mathbf{0} \\ \mathbf{f} \end{bmatrix}, \quad (36)$$

where $\mathbf{x}_0 = \bar{\mathbf{d}}$, $\mathbf{x}_1 = \mathbf{d}$, and $\mathbf{x}_2 = \dot{\mathbf{d}}$. Various standard explicit schemes could then be used, provided that \mathbf{M} is diagonal [46]. Here, we favor an explicit fourth-order Runge–Kutta (RK-4) method. Based on various numerical experiments we performed, we found out that, for the RK-4, $\Delta t < 0.8 \frac{\Delta x}{c_p}$ ensures stability on uniform grids, where Δx is the minimum distance between two grid points and c_p is the maximum compression wave velocity over an element. If, for a certain choice of time step, a simulation with displacement-only finite elements is stable, then the associated simulation

Table II. Legendre–Gauss–Lobatto quadrature rule.

Element	Location of nodes	Location of integration points	Weights
Quadratic	± 1.0	± 1.0	1/3
	0.0	0.0	4/3

involving the PML is also stable with the same time step. In other words, the introduction of the PML does not impose a more onerous time step choice than an interior elastodynamics problem would require.

5. SPECTRAL ELEMENTS AND EXPLICIT TIME INTEGRATION

Hyperbolic initial value problems are, in general, advanced in time by using explicit methods [18, 47]. This obviates the need for solving a large linear system, typically encountered in implicit schemes. Moreover, explicit schemes naturally lend themselves to parallel computation, which is essential when dealing with large-scale simulations in three-dimensional problems. In this section, we discuss how the matrix \mathbf{M} in the semi-discrete form (30) may be diagonalized, thus enabling explicit time-stepping via the techniques discussed in Section 4.2.

The simplest way of obtaining (discrete) diagonal mass-like matrices is by mass-lumping, as was done in [27, 48] where the authors used linear elements.^{§§} To achieve high-order accuracy, however, one may use nodal spectral elements, where numerical integration (quadrature rule) is based on the same nodes that polynomial interpolation is carried out [49, 50]. This results in (discrete) diagonal mass-like matrices, which are high-order accurate, depending on the degree of the interpolating polynomial. Herein, we use quadratic hexahedral elements (27 noded) with Legendre–Gauss–Lobatto quadrature rule (Table II).

An m point Legendre–Gauss–Lobatto rule integrates polynomials of degree up to and including $2m-3$, exactly [49]. However, to compute mass-like matrices, one needs to integrate terms with $\Phi\Phi^T$ -like components, where Φ is the vector of Lagrange interpolating polynomials (Appendix A.1). Having m interpolation nodes results in polynomials of degree $m-1$. The tensor products then involve terms of degree $2m-2$; thus, the approach relies on under-integration in order to return a (discrete) diagonal mass-like matrix. Herein, we use the Legendre–Gauss–Lobatto rule to compute all the submatrices presented in (31).

We remark that integration of mass-like matrices must be carried out consistently. This means that the same quadrature rule must be used to compute \mathbf{M}_{RD} , \mathbf{M}_i , \mathbf{N}_i , $i = a, b, c, d$ in (31), thus rendering all these matrices diagonal. Choosing a scheme that diagonalizes the mass-like matrix \mathbf{M} in (31), whether done by conventional mass-lumping or via spectral elements, while not applying the same scheme uniformly to all mass-like matrices, will result in instabilities, as it has also been reported in [27, 51].

6. A SYMMETRIC FORMULATION

In Section 3, we discussed a non-symmetric PML formulation that can be integrated explicitly in time. In this section, we discuss an alternative formulation that results in a symmetric semi-discrete form, which would require an implicit time-integration scheme due to a non-diagonal mass-like matrix. The key difference with the Section 3 formulation is the handling of the combined constitutive and kinematic equations. To this end, we keep the equilibrium equation in (8a) intact but express (8b) in a different form.

^{§§}By contrast to classical Galerkin finite elements, a finite difference formulation automatically yields diagonal mass-like matrices; see [46] for instance.

Similar to what was performed in [52], we start with the constitutive and kinematic equations in the time domain

$$\mathcal{S} = \mathcal{C}[\mathcal{E}], \quad (37a)$$

$$\mathcal{E} = \frac{1}{2} [\nabla \mathbf{u} + (\nabla \mathbf{u})^T], \quad (37b)$$

where \mathcal{E} is the strain tensor and \mathcal{C} is the fourth-order constitutive tensor. For an isotropic medium, $\mathcal{C}[\mathcal{E}] = 2\mu\mathcal{E} + \lambda(\text{tr}\mathcal{E})\mathcal{I}$. Taking the Fourier transform of (37), there results

$$\hat{\mathcal{S}} = \mathcal{C}[\hat{\mathcal{E}}], \quad (38a)$$

$$\hat{\mathcal{E}} = \frac{1}{2} [\nabla \hat{\mathbf{u}} + (\nabla \hat{\mathbf{u}})^T]. \quad (38b)$$

By writing (38b) in the stretched coordinate system and by using (4), we obtain

$$\hat{\mathcal{E}} = \frac{1}{2} \left\{ (\nabla \hat{\mathbf{u}}) \begin{bmatrix} \frac{1}{\lambda_x} & 0 & 0 \\ 0 & \frac{1}{\lambda_y} & 0 \\ 0 & 0 & \frac{1}{\lambda_z} \end{bmatrix} + \begin{bmatrix} \frac{1}{\lambda_x} & 0 & 0 \\ 0 & \frac{1}{\lambda_y} & 0 \\ 0 & 0 & \frac{1}{\lambda_z} \end{bmatrix} (\nabla \hat{\mathbf{u}})^T \right\}. \quad (39)$$

Multiplying (39) by $\lambda_x \lambda_y \lambda_z$ results in

$$\lambda_x \lambda_y \lambda_z \hat{\mathcal{E}} = \frac{1}{2} [(\nabla \hat{\mathbf{u}}) \Lambda + \Lambda (\nabla \hat{\mathbf{u}})^T]. \quad (40)$$

By multiplying (40) by $(i\omega)^2$ and by using (13) and (2), we obtain

$$\begin{aligned} (i\omega)^2 a \hat{\mathcal{E}} + i\omega b \hat{\mathcal{E}} + c \hat{\mathcal{E}} + \frac{1}{i\omega} d \hat{\mathcal{E}} &= \frac{1}{2} (i\omega)^2 [(\nabla \hat{\mathbf{u}}) \Lambda_e + \Lambda_e (\nabla \hat{\mathbf{u}})^T] \\ &+ \frac{1}{2} i\omega [(\nabla \hat{\mathbf{u}}) \Lambda_p + \Lambda_p (\nabla \hat{\mathbf{u}})^T] \\ &+ \frac{1}{2} [(\nabla \hat{\mathbf{u}}) \Lambda_w + \Lambda_w (\nabla \hat{\mathbf{u}})^T]. \end{aligned} \quad (41)$$

Equation (41) constitutes the corresponding frequency-domain kinematic equation in the stretched coordinate system. Taking the inverse Fourier transform of (38a) and (41), there results

$$\mathcal{S} = \mathcal{C}[\mathcal{E}], \quad (42a)$$

$$\begin{aligned} a \ddot{\mathcal{E}} + b \dot{\mathcal{E}} + c \mathcal{E} + d \left(\int_0^t \mathcal{E} d\tau \right) &= \frac{1}{2} [(\nabla \ddot{\mathbf{u}}) \Lambda_e + \Lambda_e (\nabla \ddot{\mathbf{u}})^T + (\nabla \dot{\mathbf{u}}) \Lambda_p \\ &+ \Lambda_p (\nabla \dot{\mathbf{u}})^T + (\nabla \mathbf{u}) \Lambda_w + \Lambda_w (\nabla \mathbf{u})^T]. \end{aligned} \quad (42b)$$

By combining the resulting constitutive Equation (42a) with the kinematic Equation (42b) and by using the auxiliary variables introduced in (22), we obtain

$$\begin{aligned} \mathcal{D} \left[(a \ddot{\mathbf{S}} + b \dot{\mathbf{S}} + c \mathbf{S} + d \mathbf{S}) \right] &= \frac{1}{2} [(\nabla \ddot{\mathbf{u}}) \Lambda_e + \Lambda_e (\nabla \ddot{\mathbf{u}})^T + (\nabla \dot{\mathbf{u}}) \Lambda_p \\ &+ \Lambda_p (\nabla \dot{\mathbf{u}})^T + (\nabla \mathbf{u}) \Lambda_w + \Lambda_w (\nabla \mathbf{u})^T], \end{aligned} \quad (43)$$

where \mathcal{D} is the compliance tensor ($\mathcal{E} = \mathcal{D}[S]$). Equation (43) constitutes the PML combined constitutive and kinematic equations, which is equivalent to (23b).

Next, similar to what we did in Section 4.1, we take the inner product of (43) with (tensor) test function $\mathbf{T}(\mathbf{x}) \in \mathcal{L}^2(\Omega)$; there results

$$\begin{aligned} & \int_{\Omega^{\text{PML}}} \mathbf{T} : \mathcal{D} \left(a\ddot{\mathbf{S}} + b\dot{\mathbf{S}} + c\dot{\mathbf{S}} + d\mathbf{S} \right) \, d\Omega \\ &= \frac{1}{2} \int_{\Omega^{\text{PML}}} \mathbf{T} : \left[(\nabla\ddot{\mathbf{u}}) \Lambda_e + \Lambda_e (\nabla\ddot{\mathbf{u}})^T + (\nabla\dot{\mathbf{u}}) \Lambda_p + \Lambda_p (\nabla\dot{\mathbf{u}})^T + (\nabla\mathbf{u}) \Lambda_w + \Lambda_w (\nabla\mathbf{u})^T \right] \, d\Omega. \end{aligned} \tag{44}$$

Upon discretization of (26a) and (44) via (28)-(29), we obtain a semi-discrete form

$$\mathbf{M}_s \ddot{\mathbf{d}} + \mathbf{C}_s \dot{\mathbf{d}} + \mathbf{K}_s \mathbf{d} + \mathbf{G}_s \mathbf{d} = \mathbf{f}, \tag{45}$$

with the following definition for system matrices:

$$\mathbf{M}_s = \begin{bmatrix} \bar{\mathbf{M}}_{\text{RD}} + \bar{\mathbf{M}}_a & \mathbf{0} \\ \mathbf{0} & -\mathbf{N}_a \end{bmatrix}, \quad \mathbf{C}_s = \begin{bmatrix} \bar{\mathbf{M}}_b & \bar{\mathbf{A}}_e \\ \bar{\mathbf{A}}_e^T & -\mathbf{N}_b \end{bmatrix}, \tag{46a}$$

$$\mathbf{K}_s = \begin{bmatrix} \bar{\mathbf{K}}_{\text{RD}} + \bar{\mathbf{M}}_c & \bar{\mathbf{A}}_p \\ \bar{\mathbf{A}}_p^T & -\mathbf{N}_c \end{bmatrix}, \quad \mathbf{G}_s = \begin{bmatrix} \bar{\mathbf{M}}_d & \bar{\mathbf{A}}_w \\ \bar{\mathbf{A}}_w^T & -\mathbf{N}_d \end{bmatrix}, \tag{46b}$$

$$\mathbf{d} = [\mathbf{U} \ \boldsymbol{\Sigma}]^T, \quad \mathbf{f} = [\bar{\mathbf{f}}_{\text{RD}} \ \mathbf{0}^T], \tag{46c}$$

where a bar denotes matrix extension to encompass all the displacement degrees-of-freedom; \mathbf{M}_i , $i = a, b, c, d$ are PML matrices defined in (A.2b), and \mathbf{N}_i , $i = a, b, c, d$, \mathbf{A}_i , $i = e, p, w$ are defined in (A.7) and (A.8), respectively. Moreover, similar to what we did in Section 4.2, (45) can be expressed similarly to (32) by taking into account (32b) therefore obviating the temporal differentiation of the forcing term:

$$\mathbf{M}_s \ddot{\mathbf{d}} + \mathbf{C}_s \dot{\mathbf{d}} + \mathbf{K}_s \mathbf{d} + \mathbf{G}_s \bar{\mathbf{d}} = \mathbf{f}. \tag{47}$$

System matrices defined in (46a)–(46b) are now *symmetric* and *indefinite* by contrast to (31a)–(31b). They can become positive definite if one multiplies their lower blocks by a minus sign, at the expense of losing symmetry. We refer to [29, 53] for details.

We remark that \mathbf{N}_a in \mathbf{M} is a block penta-diagonal matrix; this entails an implicit time-integration scheme for the semi-discrete form. The extended Newmark method discussed in Section 4.2 could then be used for time-stepping, which necessitates factorization of a symmetric matrix.

7. GENERALIZATION FOR M-PML

The aforementioned derivations are based on using the classical stretching function (2), where stretching is enforced only in the direction perpendicular to the PML interface. It has been reported that, in two dimensions and under certain parameterizations, this stretching function creates spurious growths when waves travel along the interface, thus leading to numerical instability. In an attempt to stabilize the PML (in 2D), Meza-Fajardo and Papageorgiou [37] proposed coordinate stretching in all directions within the PML buffer, leading to the, so-called, M-PML.

Herein, we show that by making minimal modifications, our framework can also accommodate the M-PML. We focus on the ‘right’ PML buffer zone first, that is, the volume contained in $x_0 \leq x \leq x_t$ (see Figure 1 with s replaced by x); extending the ideas to the zones where two or three

layers intersect is straightforward and can be accomplished by using superposition. We stretch the physical coordinates according to

$$\tilde{x} = x_0 + \int_{x_0}^x \left[\alpha_x(x') + \frac{1}{i\omega} \beta_x(x') \right] dx', \quad (48a)$$

$$\tilde{y} = y_0 + \int_{y_0}^y \left[\alpha_y(x) + \frac{1}{i\omega} \beta_y(x) \right] dy', \quad (48b)$$

$$\tilde{z} = z_0 + \int_{z_0}^z \left[\alpha_z(x) + \frac{1}{i\omega} \beta_z(x) \right] dz'. \quad (48c)$$

where $\alpha_y, \alpha_z, \beta_y,$ and β_z are functions of x only and are defined as

$$\alpha_y(x) = 1 + \varrho \alpha_o \left[\frac{(x - x_o)n_x}{L_{\text{PML}}} \right]^m, \quad \beta_y(x) = \varrho \beta_x(x), \quad (49a)$$

$$\alpha_z(x) = 1 + \varrho \alpha_o \left[\frac{(x - x_o)n_x}{L_{\text{PML}}} \right]^m, \quad \beta_z(x) = \varrho \beta_x(x), \quad (49b)$$

where ϱ is a proportionality constant and n_x is the outward unit normal at the interface, similar to n_s in Figure 1; α_x and β_x are defined in (5). We remark that $\alpha_y, \alpha_z, \beta_y,$ and β_z would have been identically zero in the right buffer had we used the classical stretching. Applying the fundamental theorem of calculus to (48) results in

$$\lambda_x := \frac{\partial \tilde{x}}{\partial x} = \alpha_x(x) + \frac{1}{i\omega} \beta_x(x), \quad (50a)$$

$$\lambda_y := \frac{\partial \tilde{y}}{\partial y} = \alpha_y(x) + \frac{1}{i\omega} \beta_y(x), \quad (50b)$$

$$\lambda_z := \frac{\partial \tilde{z}}{\partial z} = \alpha_z(x) + \frac{1}{i\omega} \beta_z(x). \quad (50c)$$

These are the stretching functions the authors used in [41]. However, the definition of the stretched gradient operator in Equation (3) in [41] requires additional terms, which the authors had not included. For example, the derivative with respect to \tilde{x} should read

$$\frac{\partial(\cdot)}{\partial \tilde{x}} = \frac{\partial(\cdot)}{\partial x} \frac{\partial x}{\partial \tilde{x}} + \frac{\partial(\cdot)}{\partial y} \frac{\partial y}{\partial \tilde{x}} + \frac{\partial(\cdot)}{\partial z} \frac{\partial z}{\partial \tilde{x}} \quad (51a)$$

$$= \frac{1}{\lambda_x} \frac{\partial(\cdot)}{\partial x} - \frac{\lambda_{yx}}{\lambda_x \lambda_y} \frac{\partial(\cdot)}{\partial y} - \frac{\lambda_{zx}}{\lambda_x \lambda_z} \frac{\partial(\cdot)}{\partial z}, \quad (51b)$$

instead of the expression given in [41], which reads

$$\frac{\partial(\cdot)}{\partial \tilde{x}} = \frac{1}{\lambda_x} \frac{\partial(\cdot)}{\partial x}. \quad (52a)$$

In (51), the cross-derivative terms are defined as

$$\lambda_{yx} := \frac{\partial \tilde{y}}{\partial x} = \left(\frac{\partial}{\partial x} \alpha_y(x) + \frac{1}{i\omega} \frac{\partial}{\partial x} \beta_y(x) \right) (y - y_0), \quad (53a)$$

$$\lambda_{zx} := \frac{\partial \tilde{z}}{\partial x} = \left(\frac{\partial}{\partial x} \alpha_z(x) + \frac{1}{i\omega} \frac{\partial}{\partial x} \beta_z(x) \right) (z - z_0). \quad (53b)$$

In other words, it seems that in [37, 41], the authors have not accounted properly for the Jacobian. Thus, there are at least two possible forms of the M-PML: the *uncorrected* form in [37, 41] and the *corrected* form, which accounts for the cross-derivatives. Interestingly, the numerical

experiments we performed in two dimensions with the corrected form yielded small but non-negligible reflections from the interface. By contrast, the *uncorrected* form yielded better results, despite its unsound mathematical foundation. This has led us to adopt the approach taken in [37, 41]; accordingly, the equation pertaining to the conservation of linear momentum in the stretched coordinate system becomes

$$\mathbf{div} \left(\hat{\mathbf{S}}^T \Lambda \right) - \hat{\mathbf{S}}^T \mathbf{div} \Lambda = (i\omega)^2 \rho \lambda_x \lambda_y \lambda_z \hat{\mathbf{u}}, \quad (54)$$

which results in the following strong form:

$$\begin{aligned} \mathbf{div} \left(\ddot{\mathbf{S}}^T \Lambda_e + \dot{\mathbf{S}}^T \Lambda_p + \mathbf{S}^T \Lambda_w \right) - \left(\ddot{\mathbf{S}}^T \mathbf{div} \Lambda_e + \dot{\mathbf{S}}^T \mathbf{div} \Lambda_p + \mathbf{S}^T \mathbf{div} \Lambda_w \right) \\ = \rho (a\ddot{\mathbf{u}} + b\dot{\mathbf{u}} + c\mathbf{u} + d\mathbf{u}). \end{aligned} \quad (55)$$

The structure of the formulation pertaining to the combined constitutive and kinematic equation in the stretched coordinate system remains unaltered. Hence, for accommodating the M-PML, one only needs to replace (24b) in the strong form of the equations with (55), which, in turn, changes the definition of submatrices \mathbf{A}_{eu} , \mathbf{A}_{pu} , and \mathbf{A}_{wu} in (31). The new definition of these submatrices for the M-PML case is given in Appendix A.3.

8. NUMERICAL EXPERIMENTS

We present three numerical experiments to test the accuracy and efficacy of our hybrid formulation. The first example involves a homogeneous half-space; the second one is a horizontally layered medium with an ellipsoidal inclusion. The last example compares various formulations discussed in Sections 4.2 and 6. We compare our results against an enlarged domain^{¶¶} solution with fixed boundaries, obtained via a standard displacement-only formulation, which may be viewed as a reference solution. Because of the fixed boundaries of the enlarged domain model, reflection occurs at these boundaries; hence, we limit the comparison time up to the arrival of the reflected waves to the regular domain.

In the first two examples, we apply a surface traction on the medium, with a Ricker pulse time signature, defined as

$$T_p(t) = \frac{(0.25u^2 - 0.5)e^{-0.25u^2} - 13e^{-13.5}}{0.5 + 13e^{-13.5}} \quad \text{with } 0 \leq t \leq \frac{6\sqrt{6}}{\omega_r}, \quad (56)$$

such that

$$u = \omega_r t - 3\sqrt{6}, \quad (57)$$

where $\omega_r (= 2\pi f_r)$ denotes the characteristic central circular frequency of the pulse. Here, we take $f_r = 15$ Hz, and the load has an amplitude of 1 kPa. The pulse time history and its corresponding Fourier spectrum are shown in Figure 4.

In order to quantify the performance of our PML formulation, we consider two metrics: (a) time history comparisons at selected nodes via evaluation of a time-dependent Euclidean norm of the error, relative to the reference solution; and (b) decay of the total energy within the regular domain.

We define the time-dependent Euclidean norm of the relative error at a point $\mathbf{x} \in \Omega^{\text{RD}}$ as

$$e(\mathbf{x}, t) = \frac{\|\mathbf{u}(\mathbf{x}, t) - \mathbf{u}_{\text{ED}}(\mathbf{x}, t)\|_2}{\max_t \|\mathbf{u}_{\text{ED}}(\mathbf{x}, t)\|_2}, \quad (58)$$

where $\mathbf{u}_{\text{ED}}(\mathbf{x}, t)$ represents the enlarged domain solution and the Euclidean norm of a vector $\mathbf{u}(\mathbf{x}, t) = [u_x(\mathbf{x}, t), u_y(\mathbf{x}, t), u_z(\mathbf{x}, t)]^T$ is defined as

$$\|\mathbf{u}(\mathbf{x}, t)\|_2 = \sqrt{(u_x(\mathbf{x}, t))^2 + (u_y(\mathbf{x}, t))^2 + (u_z(\mathbf{x}, t))^2}. \quad (59)$$

^{¶¶}Denoted by Ω^{ED} , such that $\Omega^{\text{RD}} \subset \Omega^{\text{ED}}$.

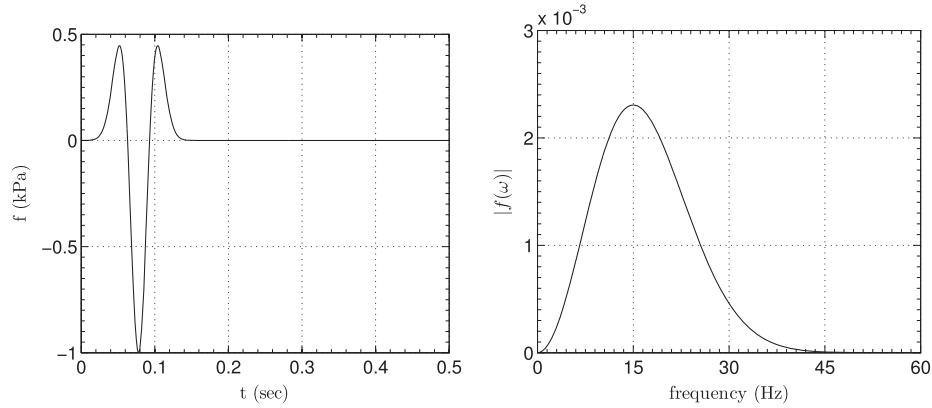


Figure 4. Ricker pulse time history and its Fourier spectrum.

The energy introduced into the system through the loading is carried via waves, which then enter the PML buffer and attenuate. Therefore, an effective PML ought to result in the rapid decay of energy. The total energy of the system can be computed at any time via

$$E_t(t) = \frac{1}{2} \int_{\Omega^{\text{RD}}} \rho(\mathbf{x}) [\dot{\mathbf{u}}^T(\mathbf{x}, t) \dot{\mathbf{u}}(\mathbf{x}, t)] \, d\Omega + \frac{1}{2} \int_{\Omega^{\text{RD}}} [\boldsymbol{\sigma}^T(\mathbf{x}, t) \boldsymbol{\epsilon}(\mathbf{x}, t)] \, d\Omega, \quad (60)$$

where $\dot{\mathbf{u}}$ denotes the velocity vector, and $\boldsymbol{\sigma}$ and $\boldsymbol{\epsilon}$ are stress and strain vectors, respectively. We compute and compare energy only within the regular domain. Moreover, $E_t(t)$ can also be used as a stability indicator because one expects that the total energy decays monotonically for a stable formulation.

8.1. Homogeneous media

We consider a homogeneous half-space with shear wave velocity $c_s = 500$ m/s, Poisson's ratio $\nu = 0.25$, and mass density $\rho = 2000$ kg/m³, which, after truncation, is reduced to a cubic computational domain of length and width 100 m \times 100 m and 50 m depth. A 12.5-m thick PML is placed at the truncation boundaries, as shown in Figure 5. Two excitations are considered: a vertical stress load (vertical excitation) and a horizontal traction along the x -axis (horizontal excitation). The excitations have the Ricker pulse temporal variation (Figure 4) and are applied on the surface of the medium over a region $(-1.25 \text{ m} \leq x, y \leq 1.25 \text{ m})$. We carry out the simulation for each excitation separately. The interior and PML domains are discretized by quadratic hexahedral spectral elements (i.e., 27-noded bricks and quadratic–quadratic pairs of approximation for displacement and stress components in the PML) of size 1.25 m. For the PML parameters, we choose $\alpha_o = 5$, $\beta_o = 866 \text{ s}^{-1}$, and a quadratic profile for the attenuation functions, that is, $m = 2$. Using the fourth-order explicit Runge–Kutta method, discussed in Appendix B.1, with a time step of $\Delta t = 0.0006$ s, we compute the response for 2 s using the hybrid formulation corresponding to (36).

We also compute a reference solution, via a standard displacement-only formulation, for an enlarged domain of size 440 m \times 440 m \times 220 m, with fixed boundaries, using the same element type and size discussed earlier. For this example, P-wave velocity is $c_p = 866$ m/s. Therefore, it takes 0.45 s for the P-wave generated by the stress load, which is applied at the center of the surface, to hit the fixed boundaries and return to the regular domain. We use the fourth-order explicit Runge–Kutta method, with $\Delta t = 0.0006$ s for time-stepping and compute the response for 0.45 s. Table III summarizes the discretization details of the two considered models.^{‡‡‡}

^{‡‡‡}We developed a code in Fortran, using Portable, PETSc [54] to facilitate parallel implementation.

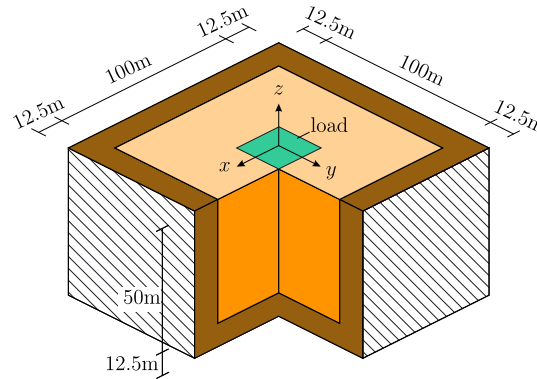


Figure 5. PML-truncated semi-infinite homogeneous media.

Table III. Discretization details of the hybrid PML and enlarged domain models.

	Elements	Nodes	Unknowns
Hybrid PML	500,000	4,080,501	24,228,426
Enlarged domain	21,807,104	175,449,825	521,884,704

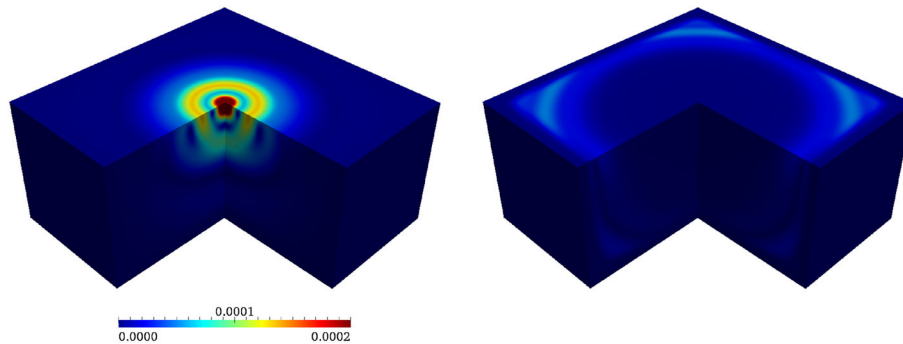


Figure 6. Snapshots of total displacement taken at $t = 0.111$ s, 0.219 s (vertical excitation).

Figure 6 displays snapshots of the total displacement at two different times for the vertical excitation. The left figure shows waves at an evolving stage, while the figure on the right demonstrates absorption of waves in the PML region. Figure 7 shows the corresponding wave motion for the horizontal excitation. No discernible reflections can be observed from the PML interface nor any residuals from the fixed-end boundaries, indicating satisfactory performance of the PML.

We compare time histories of the hybrid PML formulation against the reference solution at selected points. The location of these points are summarized in Table IV; the maximum relative error at each of these sampling points, computed using (58), is presented in the fifth and the sixth column, for the vertical and horizontal excitations, respectively. The relative error is very small and demonstrates the efficacy and success of our approach.

Figures 8 and 9 display comparison of the two responses, due to the vertical and horizontal excitation, at various sampling points. The agreement is excellent; the PML has effectively absorbed waves with practically no reflections. The response is causal, effectively dies out at around $t = 0.35$ s at all the considered points, and is free from spurious reflections.

Figure 10 shows the normalized error time history (58) due to the vertical excitation for two distinct locations: sp_3 and sp_8 . Figure 11 shows the corresponding error time history for the horizontal

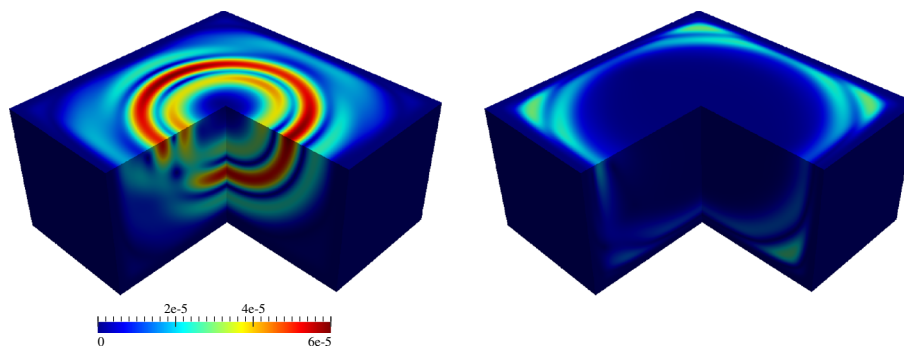


Figure 7. Snapshots of total displacement taken at $t = 0.147$ s, 0.219 s (horizontal excitation).

Table IV. Relative error at sampling points between hybrid PML and enlarged domain solutions.

Sample point	x	y	z	Error (homogeneous) Vertical excitation	Error (homogeneous) Horizontal excitation	Error (heterogeneous) Vertical excitation
sp_1	0	0	0	1.17×10^{-12}	8.77×10^{-13}	4.61×10^{-10}
sp_2	+50	0	0	2.52×10^{-8}	2.34×10^{-8}	6.07×10^{-7}
sp_3	+50	0	-25	2.89×10^{-9}	4.12×10^{-8}	2.87×10^{-6}
sp_4	+50	0	-50	1.46×10^{-7}	1.42×10^{-7}	7.03×10^{-6}
sp_5	0	0	-50	9.86×10^{-9}	2.51×10^{-9}	1.41×10^{-5}
sp_6	+50	+50	0	3.26×10^{-7}	2.16×10^{-7}	1.86×10^{-6}
sp_7	+50	+50	-25	5.50×10^{-8}	1.18×10^{-7}	6.72×10^{-6}
sp_8	+50	+50	-50	5.08×10^{-7}	5.25×10^{-7}	6.44×10^{-6}

excitation. Among all the considered locations, sp_8 has the highest error, which is only 5.08×10^{-7} for the vertical excitation and 5.25×10^{-7} for the horizontal excitation.

The total energy decay within the regular domain, because of the vertical excitation, is plotted in Figure 12, both in standard and semi-logarithmic scale for various values of β_o . Because of the limited size of the enlarged domain model, we compare the enlarged domain solution with the set of the PML solutions for various β_o only up to 0.45 s, because for $t > 0.45$ s, the reflections from the enlarged domain's fixed boundaries would have traveled back to the regular domain. The agreement is excellent, and no difference can be observed. For $\beta_o = 866 \text{ s}^{-1}$, the total reduction in energy, relative to its peak value, is 14 orders of magnitude. The decay is sharp and smooth, without any discernible reflections, indicating the effectiveness and health of the PML. Figure 13 displays the corresponding decay of energy curves due to the horizontal excitation. As can be seen from the standard scale plot, most of the energy travels out of the interior domain quickly and gets absorbed in the PML effectively.

To illustrate the stability of the formulation, we run the simulation for 50,000 time steps. The total energy decay is displayed in Figure 14 and shows no numerical instability during the simulation time.

We remark that we also used M-PML terminations to conduct this numerical experiment. While the results are satisfactory in general, they are not as accurate as when using PML terminations. In fact, for all the sampling points of Table IV, the relative error remained less than 1%, except at the corner point sp_8 where the relative error is about 5%. We do not report the M-PML-based results in detail pending comprehensive investigations.

8.2. Heterogeneous media

In the second example, we study the performance of our hybrid PML formulation for a heterogeneous medium. We consider a $100 \text{ m} \times 100 \text{ m} \times 50 \text{ m}$ layered medium with an ellipsoidal inclusion, where a 12.5-m thick PML is placed at its truncation boundaries, as shown in Figure 15. The properties of the medium are

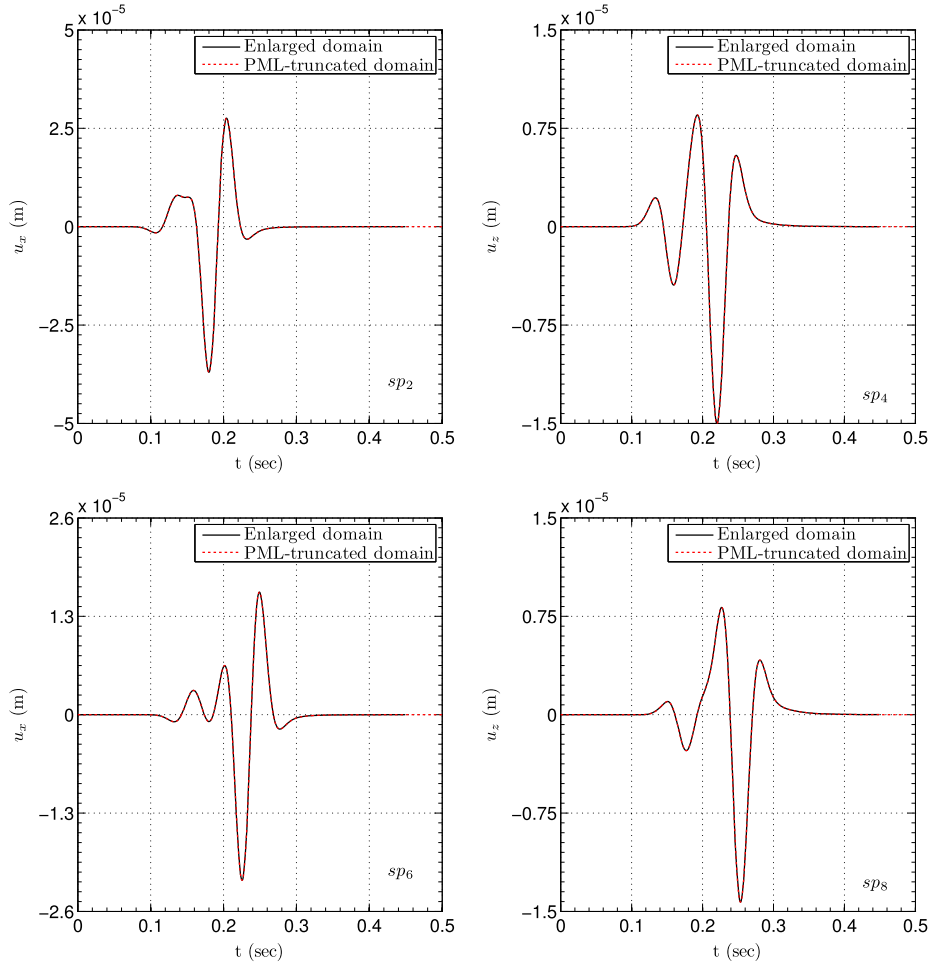


Figure 8. Comparison of displacement time histories between the enlarged and PML-truncated domain solutions at the sp_2 , sp_4 , sp_6 , and sp_8 sampling points (homogeneous case, vertical excitation).

$$c_s(z) = \begin{cases} 400 \text{ m/s}, & \text{for } -20 \text{ m} \leq z \leq 0 \text{ m}, \\ 500 \text{ m/s}, & \text{for } -50 \text{ m} \leq z < -20 \text{ m}, \\ 600 \text{ m/s}, & \text{for ellipsoidal inclusion,} \end{cases} \quad (61)$$

with mass density $\rho = 2000 \text{ kg/m}^3$, and Poisson’s ratio $\nu = 0.25$; the ellipsoidal inclusion occupies the region $\left(\frac{x-25}{15}\right)^2 + \left(\frac{y-25}{5}\right)^2 + \left(\frac{z+20}{5}\right)^2 \leq 1$. The material properties at the interfaces Γ^I are extended horizontally into the PML buffer. A vertical stress load, with the Ricker pulse temporal signature, is applied on the surface of the medium over a region $(-1.25 \text{ m} \leq x, y \leq 1.25 \text{ m})$. The problem is discretized with quadratic hexahedral elements of size 1.25 m. The PML parameters are taken as $\alpha_o = 5$, $\beta_o = 500 \text{ s}^{-1}$, and $m = 2$. To resolve the motion, we use the first-order system (36) and a fourth-order explicit Runge–Kutta method, with a time step of $\Delta t = 0.00048 \text{ s}$.

Next, a reference solution is computed by using an enlarged domain, with size and spatial discretization properties similar to the previous example, and a time step of $\Delta t = 0.00048 \text{ s}$. Table III summarizes the spatial discretization details of the problem.

To assess the performance of our hybrid PML formulation, we compare displacement time histories at selected locations against the enlarged domain solution. The sampling points, with their corresponding relative error computed via (58) are summarized in the last column of Table IV. The relative error values are higher than the previous example, which was a homogeneous medium,

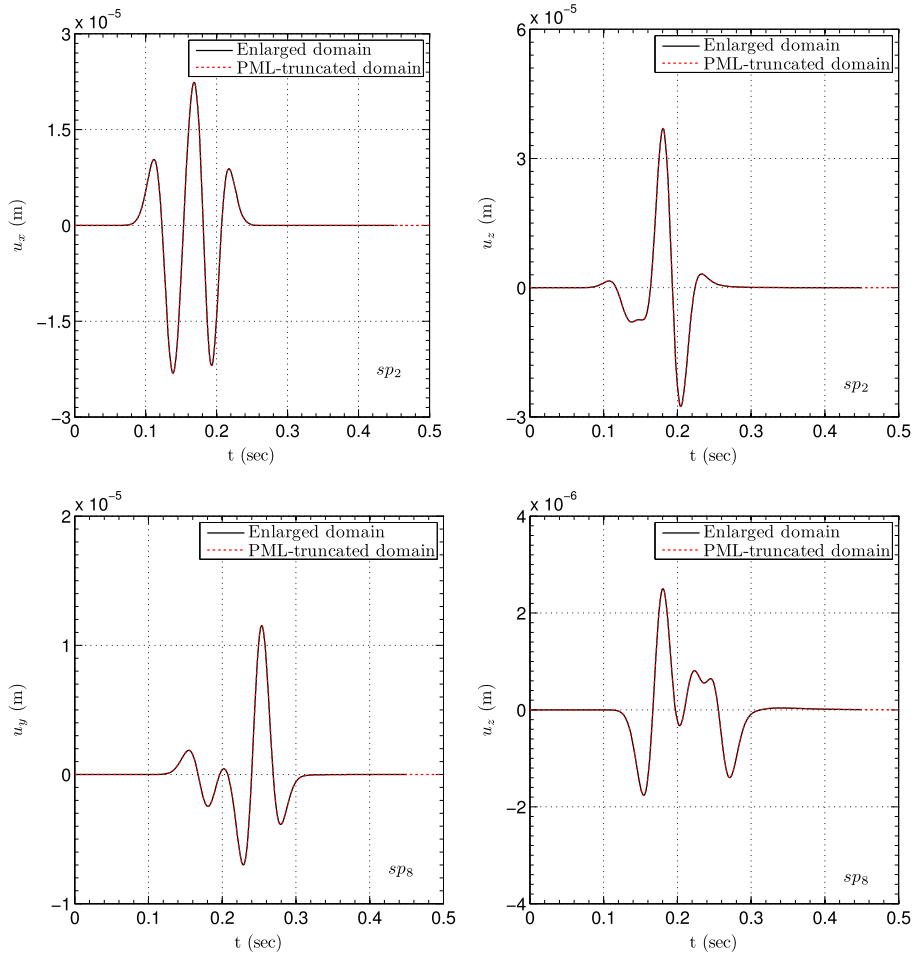


Figure 9. Comparison of displacement time histories between the enlarged and PML-truncated domain solutions at the sp_2 and sp_8 sampling points (homogeneous case, horizontal excitation).

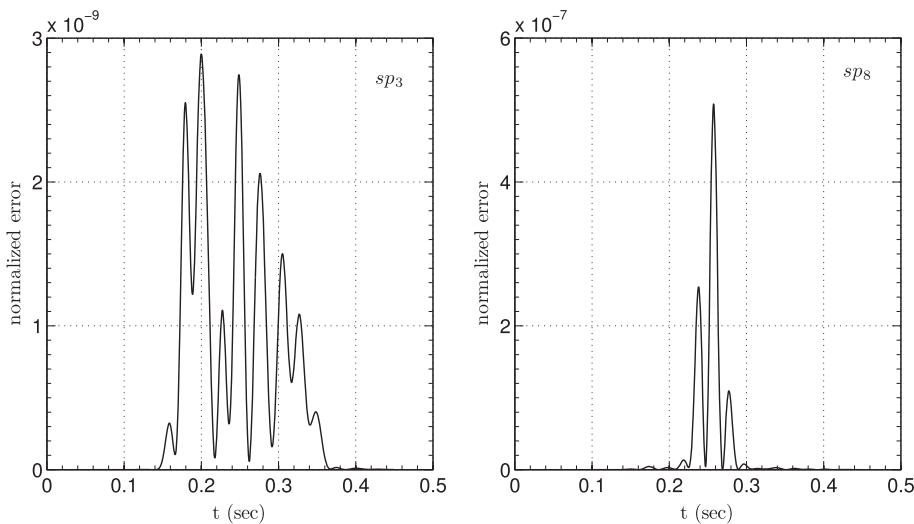


Figure 10. Relative error time history $e(\mathbf{x}, t)$ at various sampling points (homogeneous case, vertical excitation).

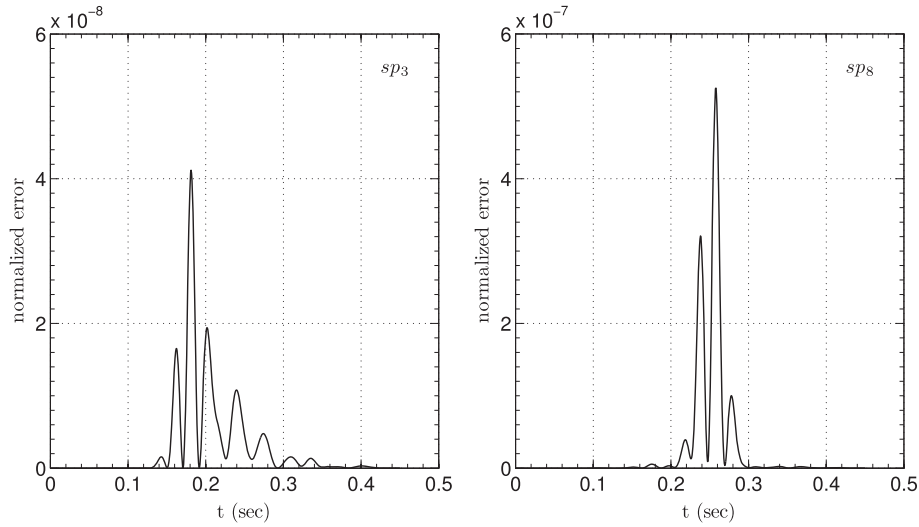


Figure 11. Relative error time history $e(\mathbf{x}, t)$ at various sampling points (homogeneous case, horizontal excitation).

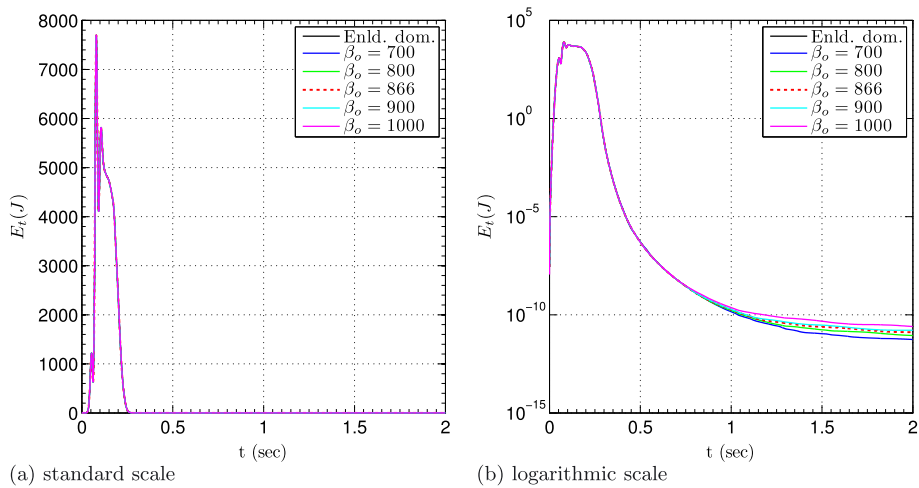


Figure 12. Total decay of energy within the regular domain for various values of β_o (homogeneous case, vertical excitation). (a) Standard scale and (b) logarithmic scale.

but still, they are very low. In fact, the highest relative error, which corresponds to sp_8 , is only 1.41×10^{-5} , which is very small in practical applications.

Snapshots of the total displacement at two different times are displayed in Figure 16. The figure on the left shows waves at an evolving stage, while the right figure indicates absorption of waves in the PML buffer zone. Notice that no discernible reflections can be seen from the PML interfaces nor any residuals from the fixed-end boundaries, a visual indication of satisfactory performance of the PML for domains involving heterogeneous material properties. Figure 17 depicts the complex wave pattern around the ellipsoidal inclusion on a cross-section through the domain situated at 20 m from the surface going through the ellipsoid’s midplane.

Various components of displacement time histories for the enlarged domain and the hybrid PML simulations are displayed in Figure 18 for selected sampling points. The agreement is excellent. The response effectively dies out at around 0.45 s. The relative error time histories are shown in Figure 19 and indicate satisfactory performance of the PML.

We compare the total energy decay within the regular domain between the PML and enlarged domain solutions. Because of the size of the enlarged domain model, the energy can only be

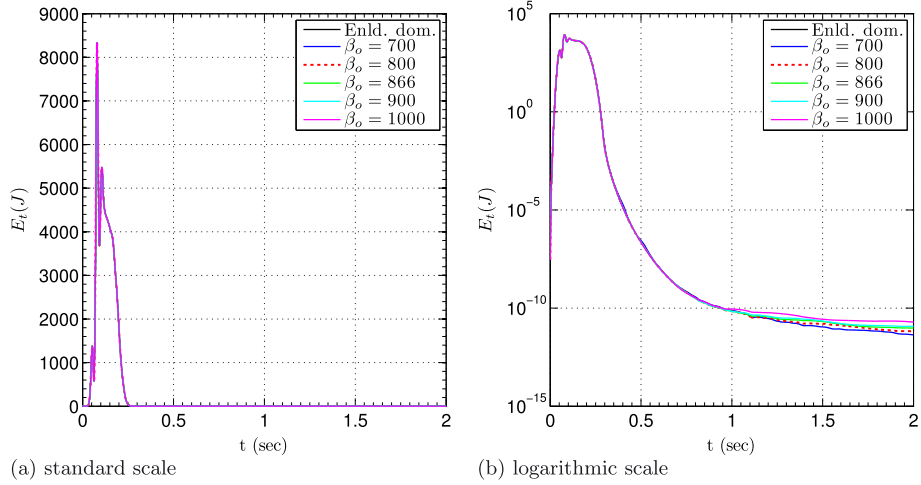


Figure 13. Total decay of energy within the regular domain for various values of β_o (homogeneous case, horizontal excitation). (a) Standard scale and (b) logarithmic scale.

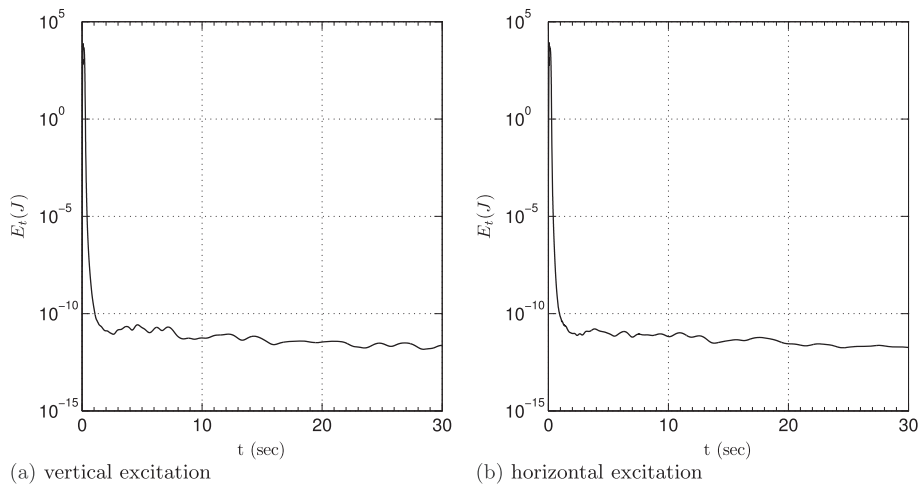


Figure 14. Total decay of energy within the regular domain for $\beta_o = 866 \text{ s}^{-1}$ (homogeneous case). (a) Vertical excitation and (b) horizontal excitation.

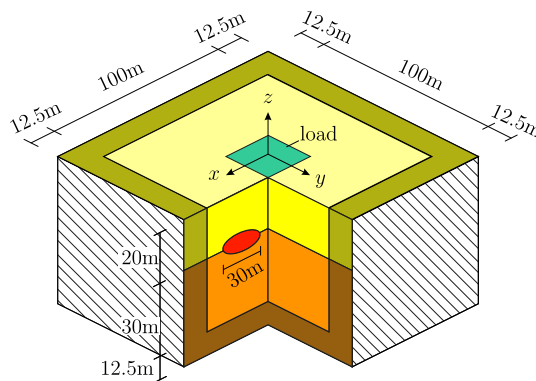


Figure 15. PML-truncated semi-infinite heterogeneous media.

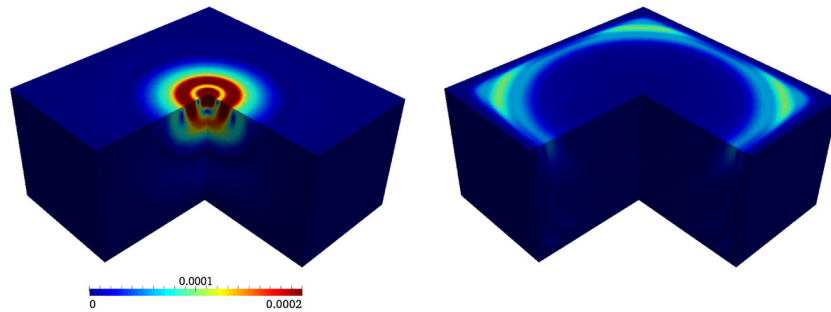


Figure 16. Snapshots of total displacement taken at $t = 0.111$ s, 0.225 s.

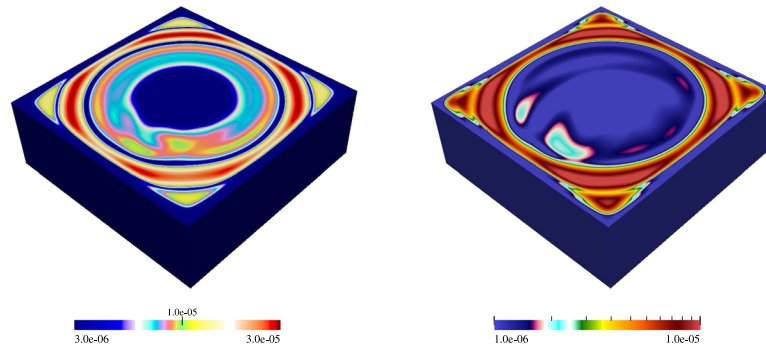


Figure 17. Snapshots of total displacement taken at $t = 0.233$ s, 0.290 s, on the $z = -20$ m domain cross-section.

computed up to 0.45 s. For the PML-truncated model, however, we allow the simulation to run for 2 s. The energy curves are presented in Figure 20. The agreement between the enlarged domain solution and the PML curves is excellent. The reduction of the total energy is 14 orders of magnitude for $\beta_o = 500 \text{ s}^{-1}$; energy decay is sharp and smooth, with no sign of reflections, signifying satisfactory performance of the PML.

Finally, to illustrate the stability of the proposed scheme, we run the simulation for 125,000 time steps. The decay of the total energy is shown in Figure 21 and shows no numerical instability during the simulation time.

8.3. Comparison of various formulations

In the previous numerical experiments, we utilized explicit time-stepping using spectral elements, which is well suited for solving large-scale problems on parallel computers. In this part, we compare alternative formulations and various time-marching schemes, discussed earlier in Sections 4.2 and 6, using the same numerical experiment considered in [27]. Specifically, we use the standard Newmark method for the second-order in time forms (34) and (35) using quadratic serendipity elements. Next, we apply the extended Newmark method to the symmetric form (47) discretized by quadratic serendipity elements. We also compute the response of the system with explicit RK-4 scheme for both PML-truncated and an enlarged domain using quadratic spectral elements. The size of the considered enlarged domain model allows simulation for up to 15 s, before reflections travel back to the interior domain. Results for PML-truncated domain models, however, are computed for 30 s. The numerical experiments are summarized in Table V.

The problem consists of a half-space with shear wave velocity $c_s = 1 \text{ m/s}$, Poisson's ratio $\nu = 0.25$, and mass density $\rho = 1 \text{ kg/m}^3$, which, after truncation, is reduced to a $1.2 \text{ m} \times 1.2 \text{ m} \times 0.2 \text{ m}$ regular domain, and 0.8-m thick PML is placed on the sides and at the bottom of the truncation boundaries, as shown in Figure 22. A uniform pressure, of the form considered in [2] (with characteristic parameters $t_d = 10 \text{ s}$, $\omega_f = 3 \text{ rad/s}$), as shown in Figure 23, is applied on the

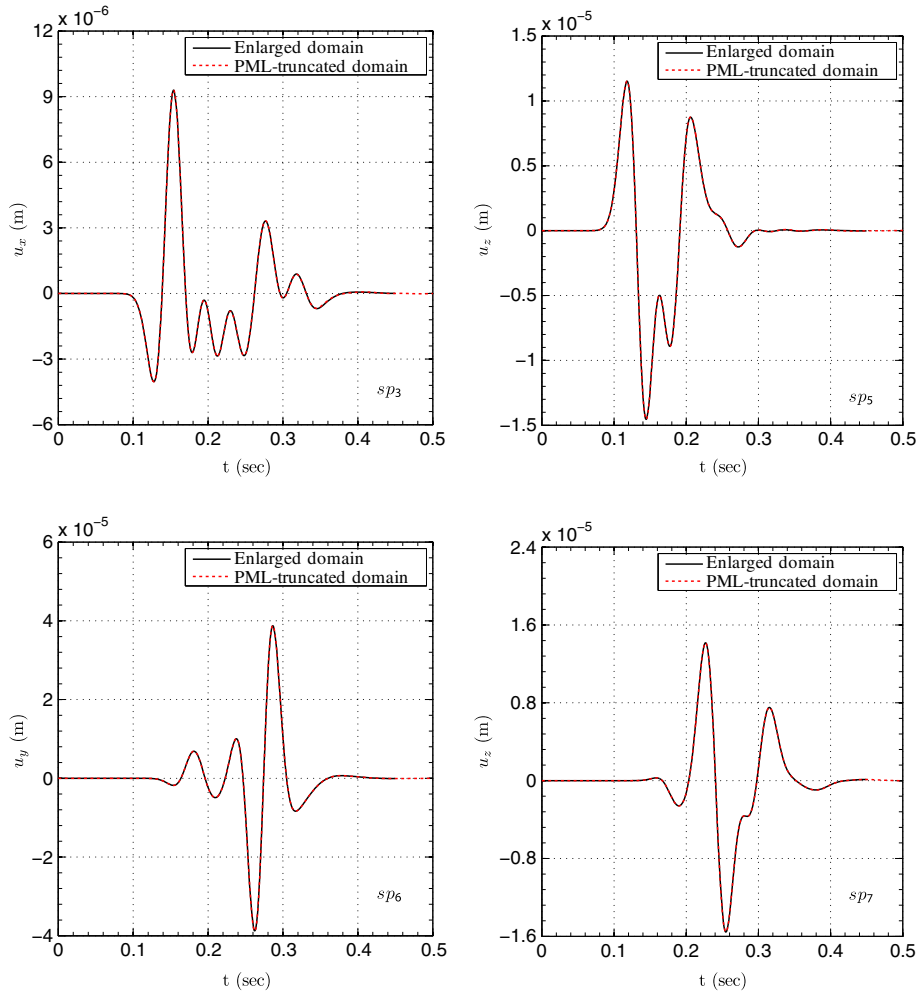


Figure 18. Comparison of displacement time histories between the enlarged and PML-truncated domain solutions at the sp_3 , sp_5 , sp_6 , and sp_7 sampling points (heterogeneous case).

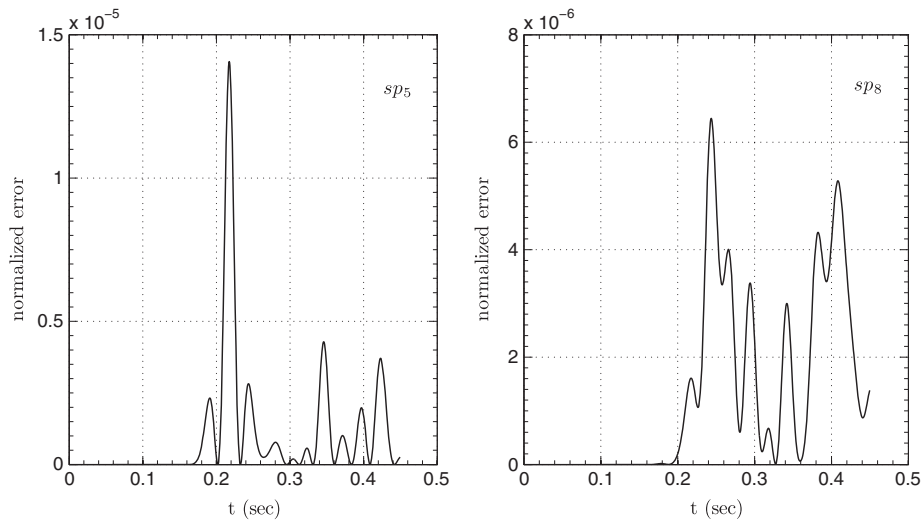


Figure 19. Relative error time history at various sampling points (heterogeneous case).

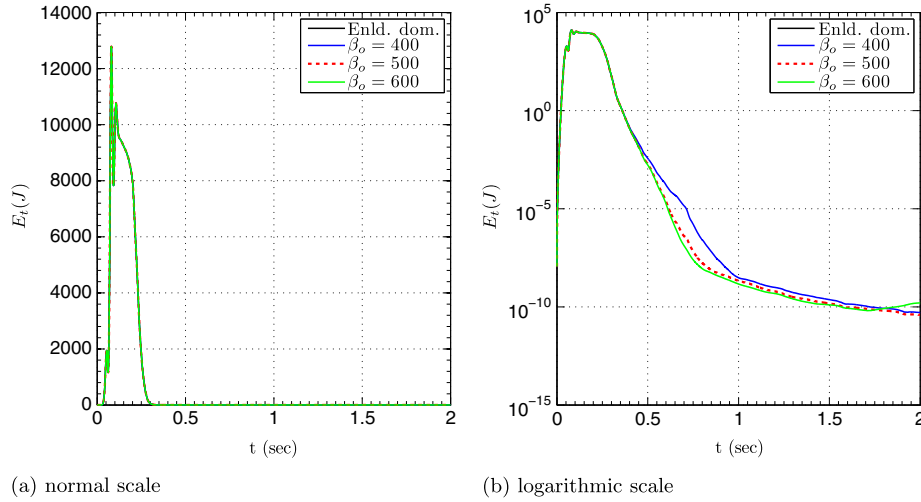


Figure 20. Total decay of energy within the regular domain for various values of β_o (heterogeneous case). (a) Normal scale and (b) logarithmic scale.

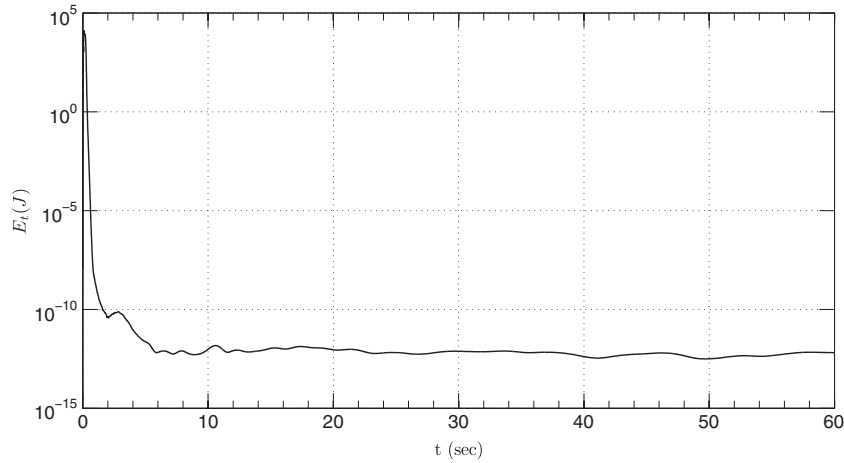


Figure 21. Total decay of energy within the regular domain for $\beta_o = 500 \text{ s}^{-1}$ (heterogeneous case).

Table V. Test cases for comparing various formulations and their corresponding relative error.

Case	Equation	Time-stepping	Element type	Error (center)	Error (corner)
UnSym-1	(34)-second order	Standard Newmark	Lagrangian 20-noded	1.73×10^{-5}	2.31×10^{-4}
UnSym-2	(35)-second order	Standard Newmark	Lagrangian 20-noded	1.73×10^{-5}	2.31×10^{-4}
Symmetric	(47)-third order	Extended Newmark	Lagrangian 20-noded	1.73×10^{-5}	2.31×10^{-4}
Explicit	(36)-first order	RK-4	Spectral 27-noded	5.03×10^{-6}	1.80×10^{-5}
Enld. dom. (No PML)	First order	RK-4	Spectral 27-noded		

surface over a region $(-1 \text{ m} \leq x, y \leq 1 \text{ m})$. Quadratic elements of size 0.2 m are used for discretizing both the interior domain and the PML buffer (i.e., quadratic–quadratic pairs of approximation for displacement and stress components in the PML). We consider $\alpha_o = 10$, $\beta_o = 20 \text{ s}^{-1}$, and $m = 2$ for the PML parameters and $\Delta t = 0.05 \text{ s}$ for temporal discretization.

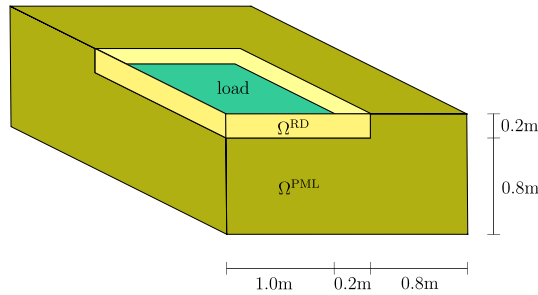


Figure 22. Quarter model of a PML-truncated semi-infinite homogeneous media.

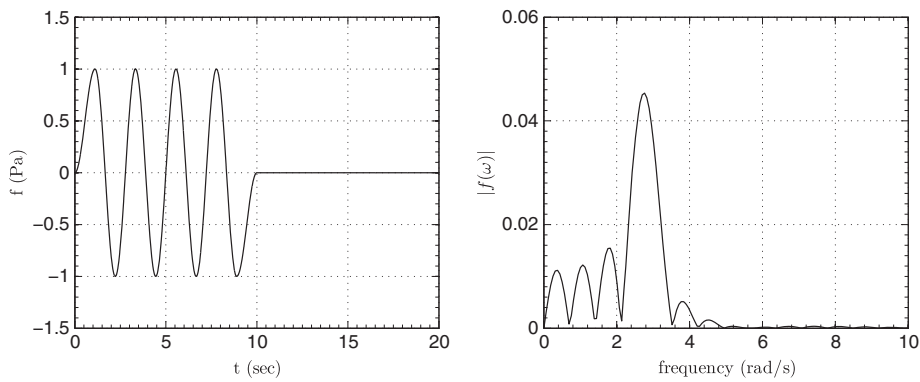


Figure 23. Surface load time history considered in Section 8.3 and its Fourier spectrum.

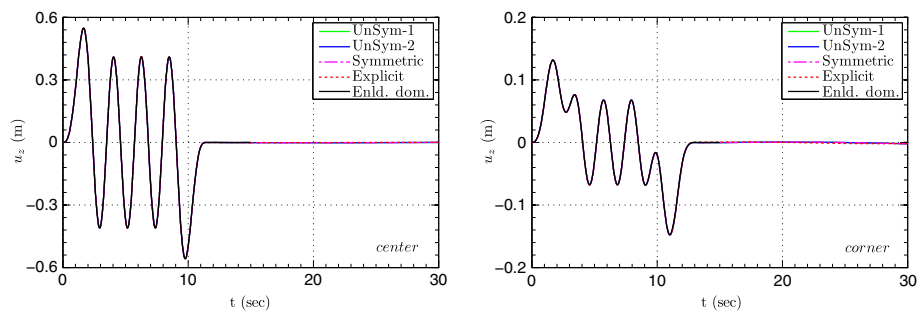


Figure 24. Comparison of displacement time histories for various cases considered in Table V.

Considering the enlarged domain solution as benchmark, we compute the maximum relative error given by (58) at the center and corner of the loading surface. These values are given in Table V and are very small, considering that PML was discretized only with four elements. The largest relative error is only 2.31×10^{-4} . The relative error for the cases using Newmark schemes are slightly greater than those using RK-4, as one would expect. The vertical component of the displacement time history for the center and corner nodes is depicted in Figure 24; the agreement is remarkable. Overall, all cases considered in Table V provide satisfactory results.

9. CONCLUSIONS

We presented various time-domain formulations for elastic wave propagation in arbitrarily heterogeneous PML-truncated media. The main contribution of this paper over the earlier work [29] is the extension to three dimensions of a hybrid formulation endowed with explicit time integration and spectral elements. Our formulation is hybrid in the sense that it uses a displacement-stress formulation for the PML buffer, coupled with a standard displacement-only formulation for the interior domain, which results in optimal computational cost and allows for the ready incorporation of the PML in existing codes. Moreover, the mixed finite element scheme for the PML buffer does not require specialized elements for Ladyzhenskaya-Babuska-Brezzi (LBB)-type stability.

The resulting semi-discrete form of the PML-truncated model is third-order in time. Several alternatives for time marching were discussed that may suit various applications. In particular, we discussed the following: (a) an explicit time-stepping scheme utilizing the Runge–Kutta method; (b) time integration via the standard Newmark scheme by recasting the semi-discrete form into a second-order system; and (c) applying an extended Newmark scheme to a fully symmetric third-order in time semi-discrete form. Numerical experiments demonstrate stability, efficacy, and satisfactory performance of the proposed schemes.

APPENDIX A: SUBMATRIX DEFINITIONS

Subscripts in the shape functions indicate derivatives.

A.1. Submatrices in Equation (31)

$$\mathbf{K}_{\text{RD}} = \int_{\Omega^{\text{RD}}} \begin{bmatrix} \mathbf{K}_{xx} & \mathbf{K}_{xy} & \mathbf{K}_{xz} \\ \mathbf{K}_{yx} & \mathbf{K}_{yy} & \mathbf{K}_{yz} \\ \mathbf{K}_{zx} & \mathbf{K}_{zy} & \mathbf{K}_{zz} \end{bmatrix} d\Omega,$$

$$\begin{aligned} \mathbf{K}_{xx} &= (\lambda + 2\mu)\Phi_x\Phi_x^T + \mu(\Phi_y\Phi_y^T + \Phi_z\Phi_z^T), \\ \mathbf{K}_{xy} &= \lambda\Phi_x\Phi_y^T + \mu\Phi_y\Phi_x^T, \\ \mathbf{K}_{xz} &= \lambda\Phi_x\Phi_z^T + \mu\Phi_z\Phi_x^T, \\ \mathbf{K}_{yx} &= \lambda\Phi_y\Phi_x^T + \mu\Phi_x\Phi_y^T, \\ \mathbf{K}_{yy} &= (\lambda + 2\mu)\Phi_y\Phi_y^T + \mu(\Phi_x\Phi_x^T + \Phi_z\Phi_z^T), \\ \mathbf{K}_{yz} &= \lambda\Phi_y\Phi_z^T + \mu\Phi_z\Phi_y^T, \\ \mathbf{K}_{zx} &= \lambda\Phi_z\Phi_x^T + \mu\Phi_x\Phi_z^T, \\ \mathbf{K}_{zy} &= \lambda\Phi_z\Phi_y^T + \mu\Phi_y\Phi_z^T, \\ \mathbf{K}_{zz} &= (\lambda + 2\mu)\Phi_z\Phi_z^T + \mu(\Phi_x\Phi_x^T + \Phi_y\Phi_y^T). \end{aligned} \quad (\text{A.1a})$$

$$\mathbf{M}_{\text{RD}} = \int_{\Omega^{\text{RD}}} \rho \text{diag}(\Phi\Phi^T, \Phi\Phi^T, \Phi\Phi^T) d\Omega. \quad (\text{A.2a})$$

$$\mathbf{M}_i = \int_{\Omega^{\text{RD}}} i \rho \text{diag}(\Phi\Phi^T, \Phi\Phi^T, \Phi\Phi^T) d\Omega, \quad i = a, b, c, d. \quad (\text{A.2b})$$

$$\mathbf{N}_i = \int_{\Omega^{\text{PML}}} i \text{diag}(\Psi\Psi^T, \Psi\Psi^T, \Psi\Psi^T, 2\Psi\Psi^T, 2\Psi\Psi^T, 2\Psi\Psi^T) d\Omega, \quad i = a, b, c, d. \quad (\text{A.2c})$$

Finally, the solution at time step $(n + 1)$ can be updated via

$$\begin{bmatrix} \mathbf{x}_0 \\ \mathbf{x}_1 \\ \mathbf{x}_2 \end{bmatrix}^{n+1} = \begin{bmatrix} \mathbf{x}_0 \\ \mathbf{x}_1 \\ \mathbf{x}_2 \end{bmatrix}^n + \frac{\Delta t}{6} \begin{bmatrix} \mathbf{k}_{10} + 2\mathbf{k}_{20} + 2\mathbf{k}_{30} + \mathbf{k}_{40} \\ \mathbf{k}_{11} + 2\mathbf{k}_{21} + 2\mathbf{k}_{31} + \mathbf{k}_{41} \\ \mathbf{k}_{12} + 2\mathbf{k}_{22} + 2\mathbf{k}_{32} + \mathbf{k}_{42} \end{bmatrix}. \quad (\text{B.4})$$

B.2. Extended Newmark method

In this part, we are concerned with the time integration of the following semi-discrete equation discussed in Sections 4.2 and 6:

$$\mathbf{M}\ddot{\mathbf{d}} + \mathbf{C}\dot{\mathbf{d}} + \mathbf{K}\mathbf{d} + \mathbf{G}\bar{\mathbf{d}} = \mathbf{f}, \quad (\text{B.5a})$$

$$\bar{\mathbf{d}} = \int_0^t \mathbf{d}(\tau)|_{\text{PML}} d\tau. \quad (\text{B.5b})$$

We discuss an extension of the Newmark method [55] for time integration of this equation. The scheme is implicit and can be applied to problems with either symmetric or unsymmetric matrices. We start with Taylor series-like expansion of the following quantities:

$$\bar{\mathbf{d}}^{n+1} = \bar{\mathbf{d}}^n + \Delta t \dot{\mathbf{d}}^n + \frac{\Delta t^2}{2} \ddot{\mathbf{d}}^n + \left(\frac{1}{6} - \alpha\right) \Delta t^3 \dddot{\mathbf{d}}^n + \alpha \Delta t^3 \ddot{\mathbf{d}}^{n+1}, \quad (\text{B.6a})$$

$$\mathbf{d}^{n+1} = \mathbf{d}^n + \Delta t \dot{\mathbf{d}}^n + \left(\frac{1}{2} - \beta\right) \Delta t^2 \ddot{\mathbf{d}}^n + \beta \Delta t^2 \ddot{\mathbf{d}}^{n+1}, \quad (\text{B.6b})$$

$$\dot{\mathbf{d}}^{n+1} = \dot{\mathbf{d}}^n + (1 - \gamma) \Delta t \ddot{\mathbf{d}}^n + \gamma \Delta t \ddot{\mathbf{d}}^{n+1}, \quad (\text{B.6c})$$

where Δt denotes the time step, superscripts (n) and $(n + 1)$ indicate current and next time steps, β and γ are the classic Newmark parameters, and α is a new parameter. Substitution of (B.6) in (B.5) at the $(n + 1)$ th time step results in the following linear system of equations

$$\hat{\mathbf{K}} \ddot{\mathbf{d}}^{n+1} = \hat{\mathbf{R}}^{n+1}, \quad (\text{B.7a})$$

where

$$\hat{\mathbf{K}} = \mathbf{M} + \gamma \Delta t \mathbf{C} + \beta \Delta t^2 \mathbf{K} + \alpha \Delta t^3 \mathbf{G}, \quad (\text{B.7b})$$

$$\begin{aligned} \hat{\mathbf{R}}^{n+1} = & \mathbf{f}^{n+1} \\ & - \mathbf{C} \left[\dot{\mathbf{d}}^n + (1 - \gamma) \Delta t \ddot{\mathbf{d}}^n \right] \\ & - \mathbf{K} \left[\mathbf{d}^n + \Delta t \dot{\mathbf{d}}^n + \left(\frac{1}{2} - \beta\right) \Delta t^2 \ddot{\mathbf{d}}^n \right] \\ & - \mathbf{G} \left[\bar{\mathbf{d}}^n + \Delta t \dot{\mathbf{d}}^n + \frac{\Delta t^2}{2} \ddot{\mathbf{d}}^n + \left(\frac{1}{6} - \alpha\right) \Delta t^3 \dddot{\mathbf{d}}^n \right]. \end{aligned} \quad (\text{B.7c})$$

Upon solving for $\ddot{\mathbf{d}}^{n+1}$ from (B.7a), $\bar{\mathbf{d}}^{n+1}$, \mathbf{d}^{n+1} , and $\dot{\mathbf{d}}^{n+1}$ can be updated using (B.6). Average-acceleration and linear-acceleration schemes correspond to taking (α, β, γ) equal to $(\frac{1}{12}, \frac{1}{4}, \frac{1}{2})$ and $(\frac{1}{24}, \frac{1}{6}, \frac{1}{2})$, respectively. Numerical results reported in Section 8.3 were computed using the average-acceleration scheme.

ACKNOWLEDGEMENT

Partial support for the authors' research has been provided by the National Science Foundation under grant awards CMMI-0619078 and CMMI-1030728. This support is gratefully acknowledged.

REFERENCES

1. Bielak J, Graves RW, Olsen KB, Taborda R, Ramirez-Guzn L, Day SM, Ely GP, Roten D, Jordan TH, Maechling PJ, Urbanic J, Cui Y, Juve G. The shakeout earthquake scenario: verification of three simulation sets. *Geophysical Journal International* 2010; **180**(1):375–404.
2. Basu U, Chopra AK. Perfectly matched layers for transient elastodynamics of unbounded domains. *International Journal of Numerical Methods in Engineering* 2004; **59**:1039–1074.
3. Epanomeritakis I, Akcelik V, Ghattas O, Bielak J. A Newton-CG method for large-scale three-dimensional elastic full-waveform seismic inversion. *Inverse Problems* 2008; **24**(3):034015.
4. Kallivokas LF, Fathi A, Kucukcoban S, Stokoe, II KH, Bielak J, Ghattas O. Site characterization using full waveform inversion. *Soil Dynamics and Earthquake Engineering* 2013; **47**:62–82.
5. Harari I, Slavutin M, Turkel E. Analytical and numerical studies of a finite element PML for the Helmholtz equation. *Journal of Computational Acoustics* 2000; **08**(01):121–137.
6. Rabinovich D, Givoli D, Bécache E. Comparison of high-order absorbing boundary conditions and perfectly matched layers in the frequency domain. *International Journal for Numerical Methods in Biomedical Engineering* 2010; **26**(10):1351–1369.
7. Collino F, Monk PB. Optimizing the perfectly matched layer. *Computer Methods in Applied Mechanics and Engineering* 1998; **164**:157–171.
8. Petropoulos PG. On the termination of the perfectly matched layer with local absorbing boundary conditions. *Journal of Computational Physics* 1998; **143**(2):665–673.
9. Bérenger JP. A perfectly matched layer for the absorption of electromagnetic waves. *Journal of Computational Physics* 1994; **114**:185–200.
10. Chew WC, Jin JM, Michielssen E. Complex coordinate system as a generalized absorbing boundary condition. *Annual Review of Progress in Applied Computational Electromagnetics*, Monterey, CA, 17–21 March 1997; 909–914. Vol. 2.
11. Chew WC, Weedon WH. A 3D perfectly matched medium from modified Maxwell's equations with stretched coordinates. *Microwave and Optical Technology Letters* 1994; **7**:599–604.
12. Teixeira FL, Chew WC. Complex space approach to perfectly matched layers: a review and some new developments. *International Journal of Numerical Modelling* 2000; **13**:441–455.
13. Chew WC, Liu QH. Perfectly matched layers for elastodynamics: a new absorbing boundary condition. *Journal of Computational Acoustics* 1996; **4**(4):341–359.
14. Collino F, Tsogka C. Application of the perfectly matched absorbing layer model to the linear elastodynamic problem in anisotropic heterogeneous media. *Geophysics* February 2001; **66**(1):294–307.
15. Hu FQ. On absorbing boundary conditions for linearized Euler equations by a perfectly matched layer. *Journal of Computational Physics* 1996; **129**:201–219.
16. Zeng YQ, He JQ, Liu QH. The application of the perfectly matched layer in numerical modeling of wave propagation in poroelastic media. *Geophysics* 2001; **66**(4):1258–1266.
17. Gedney SD. An anisotropic perfectly matched layer-absorbing medium for the truncation of FDTD lattices. *IEEE Transactions on Antennas and Propagation* December 1996; **44**(12):1630–1639.
18. Gustafsson B, Kreiss HO, Olinger J. *Time Dependent Problems and Difference Methods*. John Wiley & Sons, Inc.: New York, 1995.
19. Abarbanel S, Gottlieb D. A mathematical analysis of the PML method. *Journal of Computational Physics* 1997; **134**(2):357–363.
20. Abarbanel S, Gottlieb D. On the construction and analysis of absorbing layers in CEM. *Applied Numerical Mathematics* 1998; **27**(4):331–340. Special Issue on Absorbing Boundary Conditions.
21. Abarbanel S, Gottlieb D, Hesthaven JS. Long time behavior of the perfectly matched layer equations in computational electromagnetics. *Journal of Scientific Computing* 2002; **17**(1–4):405–422.
22. Duru K, Kreiss G. A well-posed and discretely stable perfectly matched layer for elastic wave equations in second order formulation. *Communications in Computational Physics* 2012; **11**(5):1643–1672.
23. Bécache E, Fauqueux S, Joly P. Stability of perfectly matched layers, group velocities and anisotropic waves. *Journal of Computational Physics* 2003; **188**:399–433.
24. Drossaert FH, Giannopoulos A. A nonsplit complex frequency-shifted PML based on recursive integration for FDTD modeling of elastic waves. *Geophysics* March–April 2007; **72**(2):T9–T17.
25. Komatitsch D, Martin R. An unsplit convolutional perfectly matched layer improved at grazing incidence for the seismic wave equation. *Geophysics* September–October 2007; **72**(5):SM155–SM167.
26. Wang T, Tang X. Finite-difference modeling of elastic wave propagation: a nonsplitting perfectly matched layer approach. *Geophysics* 2003; **68**(5):1749–1755.
27. Basu U. Explicit finite element perfectly matched layer for transient three-dimensional elastic waves. *International Journal for Numerical Methods in Engineering* 2009; **77**:151–176.
28. Martin R, Komatitsch D, Gedney SD. A variational formulation of a stabilized unsplit convolutional perfectly matched layer for the isotropic or anisotropic seismic wave equation. *CMES* 2008; **37**(3):274–304.
29. Kucukcoban S, Kallivokas LF. A symmetric hybrid formulation for transient wave simulations in PML-truncated heterogeneous media. *Wave Motion* 2013; **50**:57–79.
30. Hastings FD, Schneider JB, Broschat SL. Application of the perfectly matched layer (PML) absorbing boundary condition to elastic wave propagation. *Journal of the Acoustical Society of America* 1996; **100**(5):3061–3069.

31. Liu QH. Perfectly matched layers for elastic waves in cylindrical and spherical coordinates. *Journal of the Acoustical Society of America* April 1999; **105**(4):2075–2084.
32. Bécache E, Joly P, Tsogka C. Fictitious domains, mixed finite elements and perfectly matched layers for 2D elastic wave propagation. *Journal of Computational Acoustics* September 2001; **9**(3):1175–1202.
33. Festa G, Nielsen S. PML absorbing boundaries. *Bulletin of the Seismological Society of America* April 2003; **93**(2):891–903.
34. Komatitsch D, Tromp J. A perfectly matched layer absorbing boundary condition for the second-order seismic wave equation. *Geophysical Journal International* 2003; **154**:146–153.
35. Cohen G, Fauqueux S. Mixed spectral finite elements for the linear elasticity system in unbounded domains. *SIAM Journal of Scientific Computing* 2005; **26**(3):864–884.
36. Festa G, Vilotte JP. The Newmark scheme as velocity-stress time-staggering: an efficient PML implementation for spectral element simulations of elastodynamics. *Geophysical Journal International* 2005; **161**:789–812.
37. Meza-Fajardo KC, Papageorgiou AS. A nonconvolutional, split-field, perfectly matched layer for wave propagation in isotropic and anisotropic elastic media: stability analysis. *Bulletin of the Seismological Society of America* August 2008; **98**(4):1811–1836.
38. Correia D, Jin JM. Performance of regular PML, CFS-PML, and second-order PML for waveguide problems. *Microwave and Optical Technology Letters* October 2006; **48**(10):2121–2126.
39. Dmitriev MN, Lisitsa VV. Application of M-PML reflectionless boundary conditions to the numerical simulation of wave propagation in anisotropic media. Part I: reflectivity. *Numerical Analysis and Applications* 2011; **4**(4):271–280.
40. Dmitriev MN, Lisitsa VV. Application of M-PML absorbing boundary conditions to the numerical simulation of wave propagation in anisotropic media. Part II: stability. *Numerical Analysis and Applications* 2012; **5**(1):36–44.
41. Meza-Fajardo KC, Papageorgiou AS. Study of the accuracy of the multi-axial perfectly matched layer for the elastic-wave equation. *Bulletin of the Seismological Society of America* December 2012; **102**(6):2458–2467.
42. Ping P, Zhang Y, Xu Y. A multi-axial perfectly matched layer (M-PML) for the long-time simulation of elastic wave propagation in the second-order equations. *Journal of Applied Geophysics* 2014; **101**:124–135.
43. Kucukcoban S, Kallivokas LF. Mixed perfectly-matched-layers for direct transient analysis in 2D elastic heterogeneous media. *Computer Methods in Applied Mechanics and Engineering* 2011; **200**(1–4):57–76.
44. Kallivokas LF, Bielak J, MacCamy RC. A simple impedance-infinite element for the finite element solution of the three-dimensional wave equation in unbounded domains. *Computer Methods in Applied Mechanics and Engineering* 1997; **147**:235–262.
45. Brezzi F. A survey of mixed finite element methods. In *Finite Elements Theory and Application*, Dwoyer DL, Hussaini MY, Voigt RG (eds). Springer-Verlag: New York, 1988; 34–49.
46. Quarteroni A, Sacco R, Saleri F. *Numerical Mathematics* (2nd edn), Texts in Applied Mathematics. Springer: Berlin Heidelberg, 2007.
47. Quarteroni A, Valli A. *Numerical Approximation of Partial Differential Equations*, Springer Series in Computational Mathematics. Springer: Berlin Heidelberg, 2008.
48. Bao H, Bielak J, Ghattas O, Kallivokas LF, O'Hallaron DR, Shewchuk JR, Xu J. Large-scale simulation of elastic wave propagation in heterogeneous media on parallel computers. *Computer Methods in Applied Mechanics and Engineering* 1998; **152**:85–102.
49. Kopriva DA. *Implementing Spectral Methods for Partial Differential Equations*. Springer, 2009.
50. Wilcox LC, Stadler G, Burstedde C, Ghattas O. A high-order discontinuous Galerkin method for wave propagation through coupled elastic-acoustic media. *Journal of Computational Physics* 2010; **229**:9373–9396.
51. Matzen R. An efficient finite element time-domain formulation for the elastic second-order wave equation: a non-split complex frequency shifted convolutional PML. *International Journal for Numerical Methods in Engineering* 2011; **88**(10):951–973.
52. Kucukcoban S. The inverse medium problem in PML-truncated elastic media. *Ph.D. Thesis*, The University of Texas at Austin, Austin, TX, USA, 2010.
53. Benzi M, Golub GH, Liesen J. Numerical solution of saddle point problems. *Acta Numerica* 2005; **14**:1–137.
54. Balay S, Brown J, Buschelman K, Eijkhout V, Gropp WD, Kaushik D, Knepley MG, McInnes LC, Smith BF, Zhang H. PETSc users manual. *Technical Report ANL-95/11 - Revision 3.4*, Argonne National Laboratory: Chicago, IL, USA, 2013.
55. Assimaki D, Kallivokas LF, Kang JW, Kucukcoban S. Time-domain forward and inverse modeling of lossy soils with frequency-independent Q for near-surface applications. *Soil Dynamics and Earthquake Engineering* 2012; **43**: 139–159.